Wafer-scale Aluminum Nanoplasmonic Resonators with Optimized Metal Deposition

Vladimir Liberman,[1,*] *Kenneth A. Diest,*[1] *Corey Stull,*[1] *Matthew Cook,*[1] *Donna M. Lennon,*[1] *Mordechai Rothschild*[1] *and Stefan Schoeche*[2]

[1]Lincoln Laboratory, Massachusetts Institute of Technology, Lexington, Massachusetts 02420

[2]J. A. Woollam Co., Inc., 645 M Street, Lincoln, NE 68508

[*]vlad@ll.mit.edu

ABSTRACT. Spectroscopic ellipsometry is demonstrated to be an effective technique for assessing the quality of plasmonic resonances within aluminum nanostructures deposited with multiple techniques. The resonance quality of nanoplasmonic aluminum arrays is shown to be strongly dependent on the method of aluminum deposition. Three-layer metal-dielectric-metal nanopillar arrays were fabricated in a complementary metal-oxide semiconductor (CMOS) facility, with the arrays of nanopillars separated from a continuous metal underlayer by a thin dielectric spacer, to provide optimum field enhancement. Nanostructures patterned in optimized aluminum, which had been deposited with a high temperature sputtering process followed by chemical mechanical planarization, display different resonance and depolarization behavior than nanostructures deposited by the more conventional evaporation process. Full plasmonic band diagrams are mapped over a wide range of incidence angles and wavelengths using spectroscopic ellipsometry, and compared for aluminum nanostructures fabricated with two methods. The resonators fabricated from optimized aluminum exhibit a narrower bandwidth of both plasmonic resonance and depolarization parameters, indicating a higher quality resonance due to a stronger localization of the electric field. The optimized wafer-scale aluminum plasmonics fabrication should provide a pathway towards better quality devices for sensing and light detection in the ultraviolet and blue parts of the spectrum.

INTRODUCTION

The use of aluminum metal for ultraviolet plasmonics was first proposed almost 30 years ago.[1] Because the plasma frequency of aluminum is at significantly higher energies than that of gold or silver, aluminum holds promise for UV sensing and light harvesting applications, with potential for enhanced linewidth narrowing, when compared with traditional plasmonic metals.[2] However, due to perceived deficiencies in the plasmonic response of aluminum via oxide formation and small grain sizes, aluminum plasmonics has only recently received significant attention. The recent resurgence of interest in aluminum plasmonics can be attributed to advances in deposition techniques, nanofabrication capabilities, and improvement in material quality.[3-13] Applications of aluminum plasmonics are being pursued for energy harvesting and super absorbers,[14-20] sensing,[21-24] photodetection,[25, 26] structural color,[27, 28] holography[29] and nanoantennae design.[30-40] Nevertheless, a robust underpinning of fabrication procedures, supported by advanced metrology, is still lacking and severely hinders the practical implementation of aluminum plasmonics.

Unlike plasmonic devices based on coinage metals, such as gold and silver, which are effectively banned from silicon semiconductor fabrication facilities, aluminum plasmonics can benefit from the vast infrastructure of complementary metal-oxide semiconductor (CMOS) technology that is used for the fabrication of most of today's semiconductor chips. While a number of promising applications for aluminum plasmonics have been demonstrated, these studies have not taken advantage of wafer-scale plasmonic platforms, leveraging the compatibility of aluminum with CMOS infrastructure. Here, we demonstrate fully scalable aluminum plasmonics nanoresonator fabrication that utilizes the processing capabilities of semiconductor manufacturing, including sputtering, chemical mechanical polishing, atomic layer deposition and reactively-assisted ion etching. The design is based on metal-dielectric-metal multilayer structures, proposed for strong coupling of localized and propagating plasmon modes.[41] We show that aluminum nanostructures fabricated with an optimized aluminum process, based on high-temperature sputtering and planarization, have superior plasmonic properties when compared to the nanostructures produced by conventional evaporation.

Recently, spectroscopic Mueller-matrix ellipsometry has emerged as a powerful diagnostic for mapping of localized and propagating plasmon modes, as well as for characterization of fishnet metamaterials.[42-44] As compared to polarized reflectance measurements, ellipsometry offers several advantages: a) measurements are highly accurate due to self-referencing; b) phase information in addition to amplitude information is obtained and c) full polarimetry data are readily obtained through Mueller matrix measurements. In this work, through the use of Mueller-matrix spectroscopic ellipsometry, we obtain a full plasmonic band diagram for the nanostructures. Furthermore, through the measurement of the ellipsometric depolarization parameter, we demonstrate a powerful connection between near-field plasmon localization and far-field light scattering.

RESULTS AND DISCUSSION

Nanoplasmonic resonator design

For the nanostructure design, we have chosen a three-layer periodic array of aluminum nanopillars spaced by a thin dielectric layer from a metallic mirror underlayer (
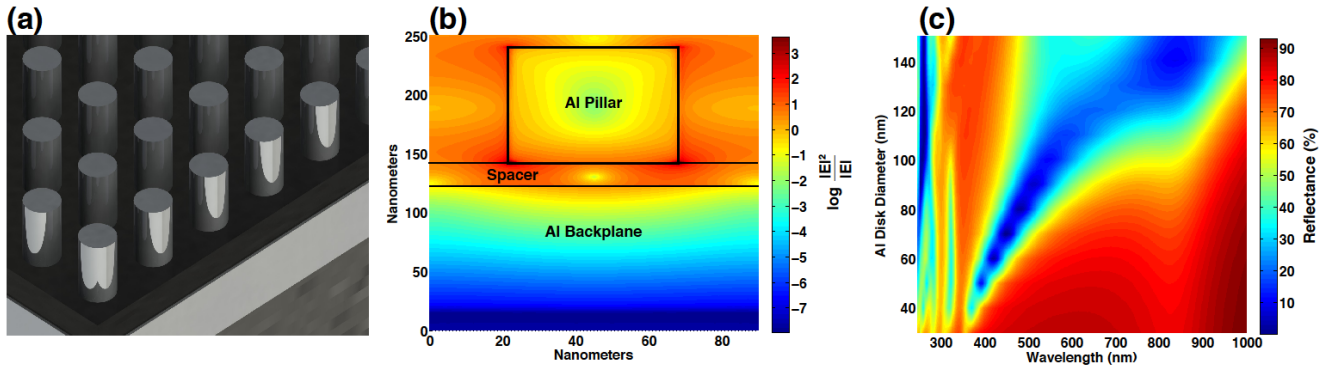

Figure 1A).[18, 41, 45, 46] Coupling light into such structures excites both localized and propagating plasmon modes. Through the interference of these modes, perfect absorption and accompanying high local field intensities are expected at resonance wavelengths. Thus, such structures are useful for both sensing applications and for the fundamental study of photon coupling into plasmonic modes.

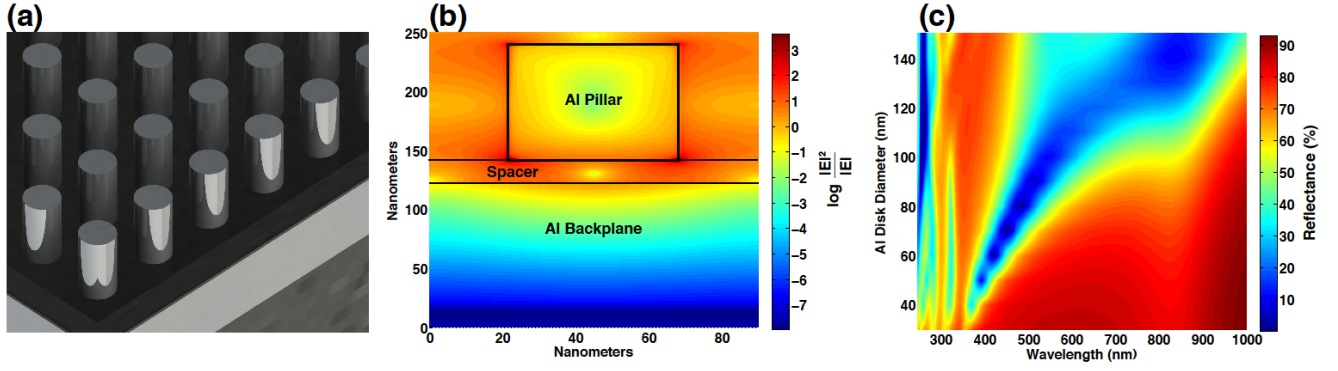We have modeled the three-layer nanoplasmonic array with full-field electromagnetic simulations (

Figure 1). **The two main modes are observed for normal incidence reflectance where the array pitch is 250 nm and the spacer layer thickness is kept constant at 20 nm (**
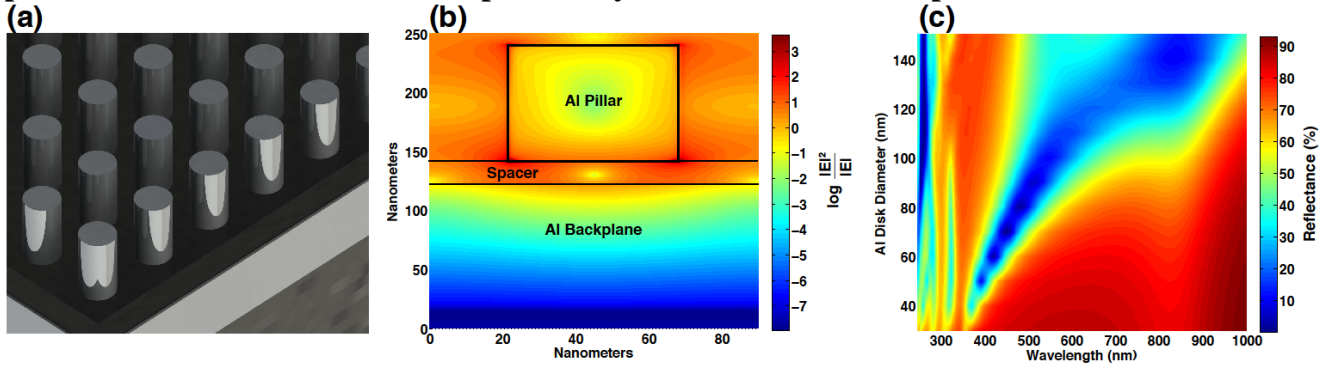

Figure **1**C). First, there is a localized surface plasmon (LSP) resonance in the visible part of the spectrum for pillar diameters around 100 nm, which shifts to the ultraviolet (UV) part of the spectrum for pillar diameters below 50 nm. Secondly, a propagating surface plasmon polariton (SPP) mode occurs near 250 nm, which is independent of pillar diameter. Additional weaker modes are observed between the wavelengths of 250 and 350 nm, and these will be discussed below. For an optimized pillar-array with a 45-nm diameter and 90-nm spacing, the LSP resonance occurs in the UV at 300 nm. A field intensity profile for such a structure is shown in
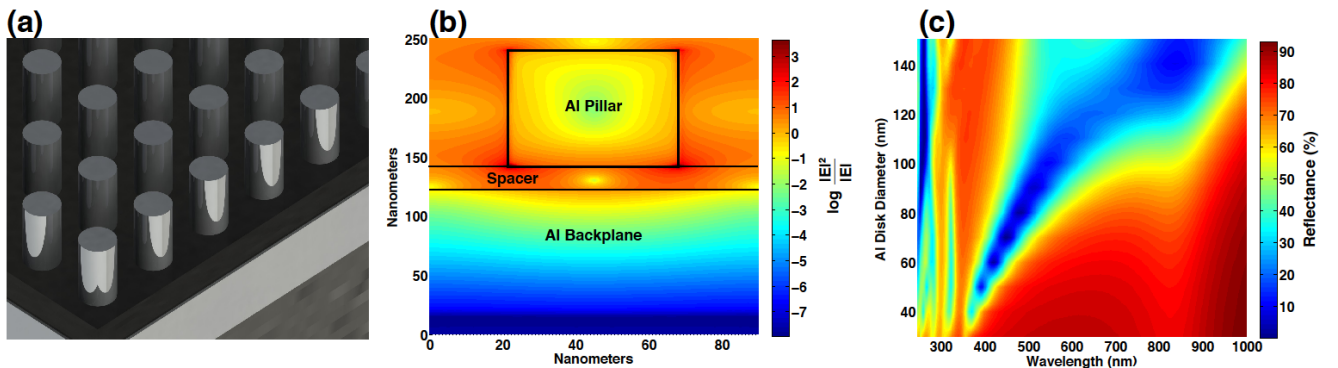
Figure **1**B as a cross-section through the center of the pillar. Large electric field enhancement is evident in the bottom corners of aluminum pillars adjacent to the dielectric spacer, with maximum field intensity exceeding 10^3, as compared to the incident field.
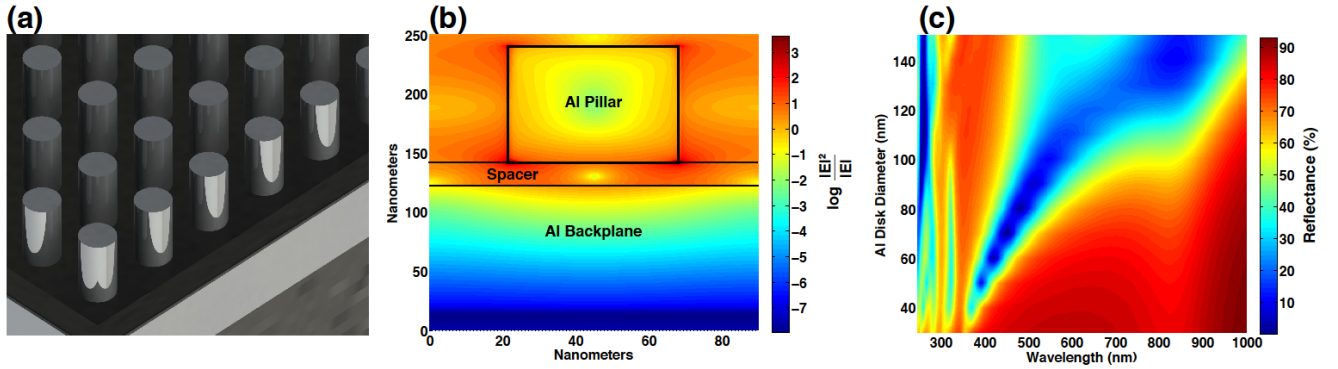

Figure 1 A. Periodic array of plasmonic nanostructures separated from a metal backplane by a thin dielectgric spacer. B. Full-field simulation of a structure cross-section, showing electric field intensity distribution. C. Predicted normal incidence reflectance as a function of nanostructure diameter and wavelength. For these simulations, optical constants for conventional evaporated aluminum are used.[4]

Wafer scale fabrication

To access UV resonances in the nanoplasmonic structures, individual post diameters below 50 nm are required (
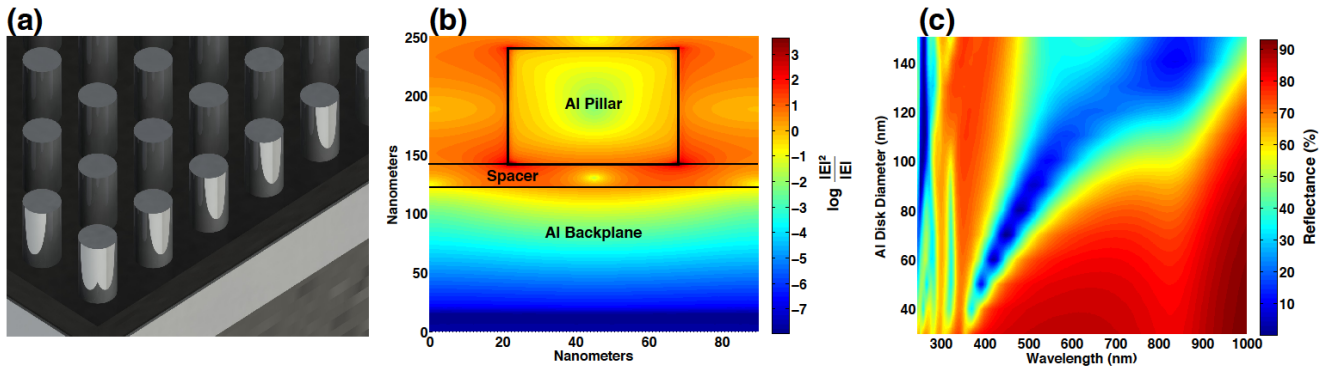

Figure **1**B & C). Such feature sizes can be readily fabricated in current semiconductor fabrication facilities. Previously, we have shown that the grain structure of conventional electron-beam evaporated aluminum films is on the length scale of the size of these resonators,[4] Due to preferential etching along metal grain boundaries, nanoscale structures with feature sizes below 50 nm and such fine grain structure are incompatible with high fidelity lithography and pattern transfer. To address the inadequacy of conventional room-temperature evaporation, we developed a wafer-scale aluminum deposition process, comprising high-temperature sputtering followed by chemical mechanical polishing (CMP) that

resulted in micron sized grains with sub-nm surface roughness. We also demonstrated that these films have a plasmonic figure-of-merit over three times higher than evaporated films throughout the visible and near-ultraviolet spectrum.[4]

In this work, we fabricated identical sets of nanopillar arrays on two separate wafers. The only difference between the two samples was the type of aluminum used: the first set of nanopillars was fabricated using aluminum deposited by high-temperature-sputtering/CMP, while the second set of nanopillars was fabricated using aluminum deposited by electron beam evaporation. To ensure that the conventional evaporated aluminum structures survived the fabrication steps, the diameter of the nanopillars was set at 75 nm, as defined using electron beam lithography. Hereafter, we refer to the first sample of aluminum arrays as "sputtered" and the second sample as "evaporated." For both samples, the pitch of the arrays was 250 nm, and the area of the arrays was 9 mm^2. Cross-sectional diagram of the fabricated unit cell is shown in Figure 2. For both samples, the aluminum backplane is fabricated with a conventional unoptimized room-temperature sputtering process.

The detailed fabrication process flow is described in the Methods section. In brief, a 20 nm thick titanium nitride layer was deposited between the top aluminum layer and the electron beam resist to protect the underlying aluminum during resist development. After lithography, the nanocone features were reactively-ion etched with a Cl_2/BCl_3 mixture. Due to the dry etch used during patterning, the resultant structures had slightly tapered sidewalls, leading to a cone-shape rather than vertical pillars (Figure 2, Figure **3**A)
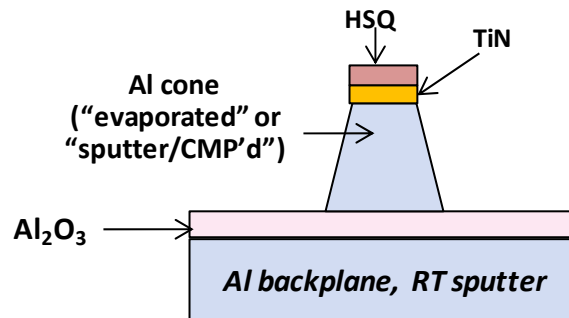

Figure 2. Cross-sectional diagram of a unit cell of a fabricated nanocone array.

Cross-sectional scanning electron microscope images of the sputtered sample are shown in
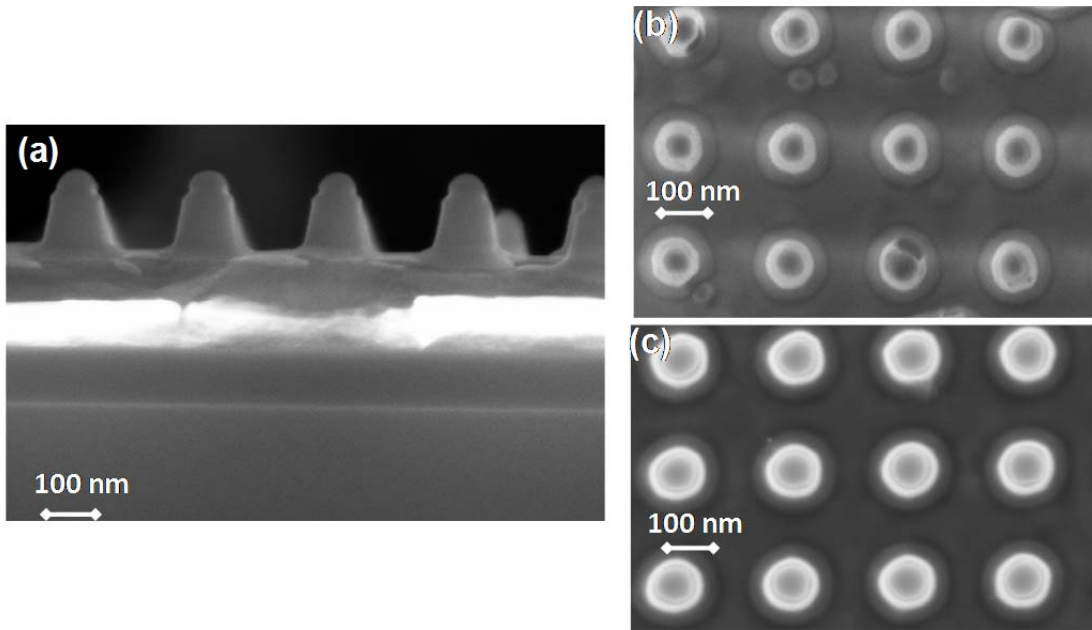

Figure **3**A. The top of the nanopillars corresponds to the feature size defined by electron beam lithography, around 75 nm. The remainder of the hydrogen silsesquioxane (HSQ) electron beam resist layer and the titanium nitride layer is visible as a rounded protrusion near the top of the nanocone. The top-down SEMs show that the evaporated cone array (
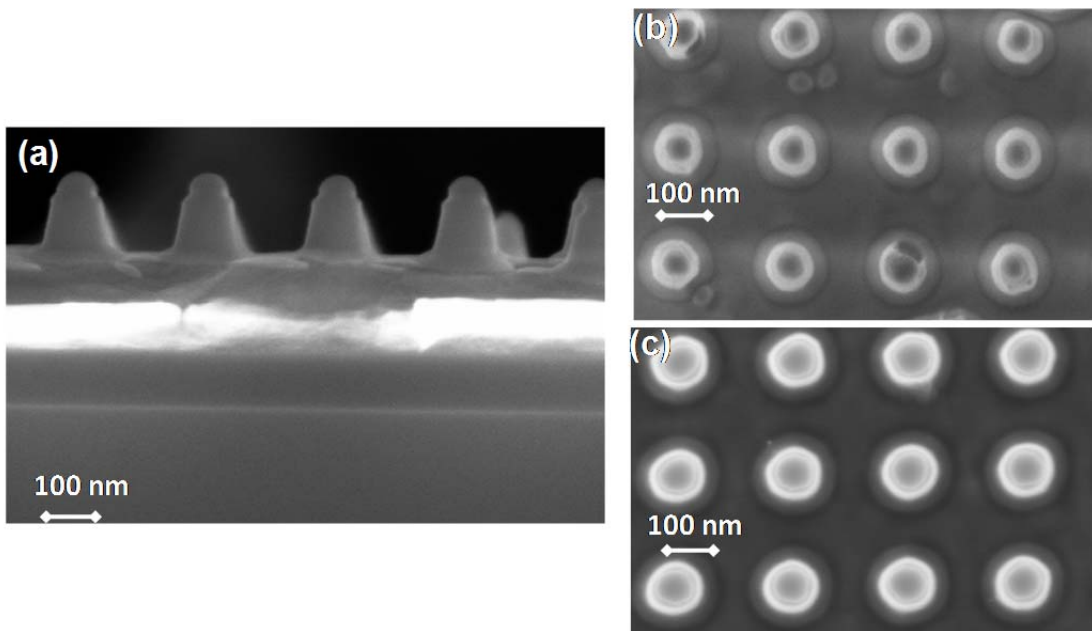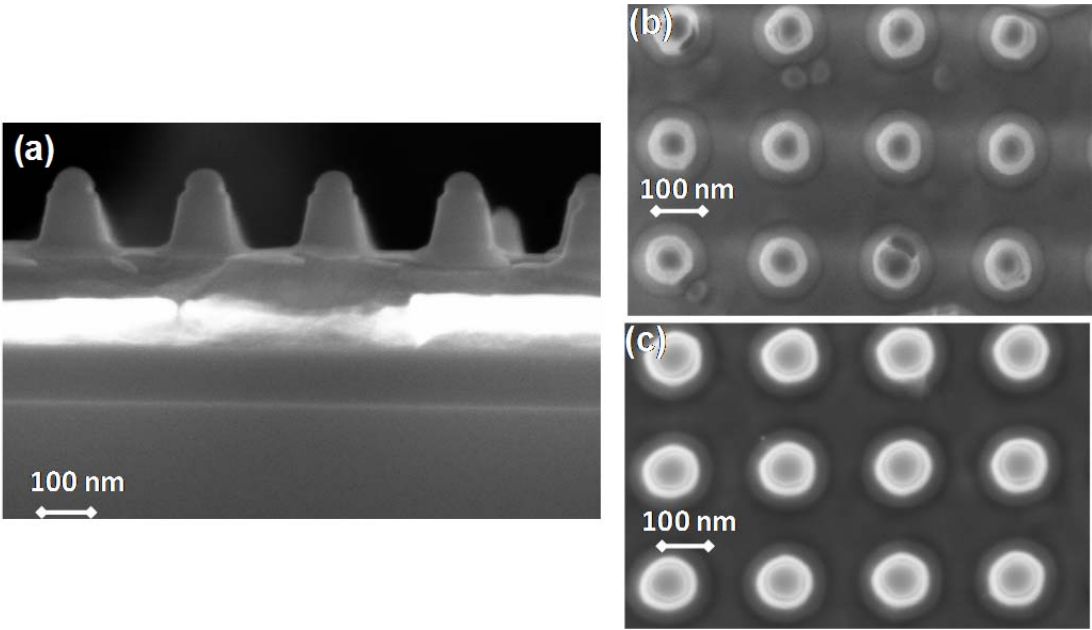
Figure **3**B) has a higher density of defects, residue and some cone asymmetry as compared to the

sputtered array (

Figure **3**C), most likely resulting from preferential etching along the large number of grain boundaries

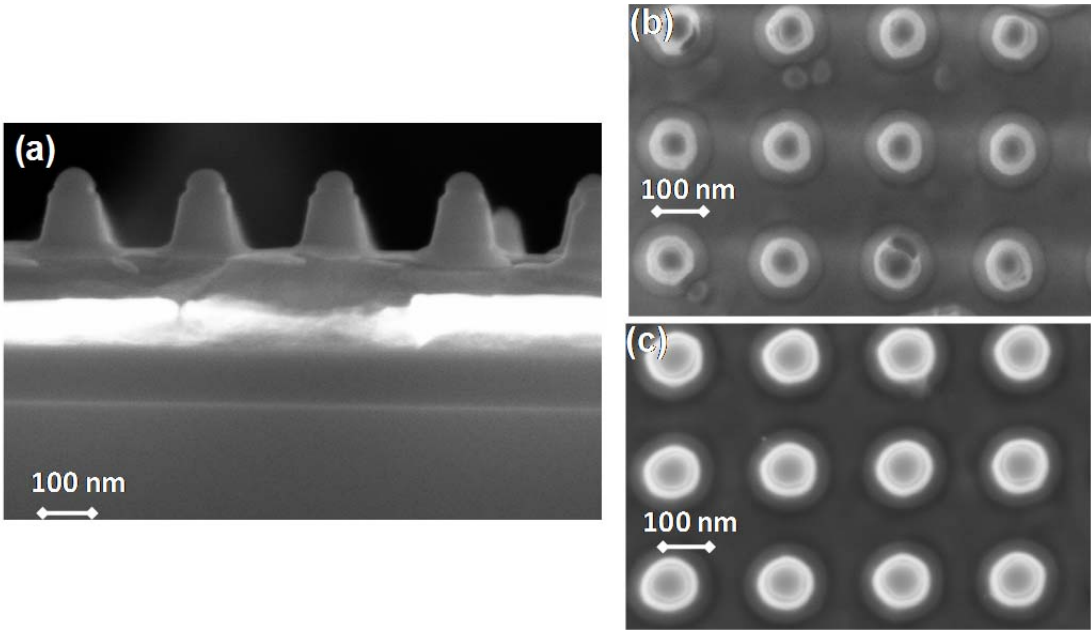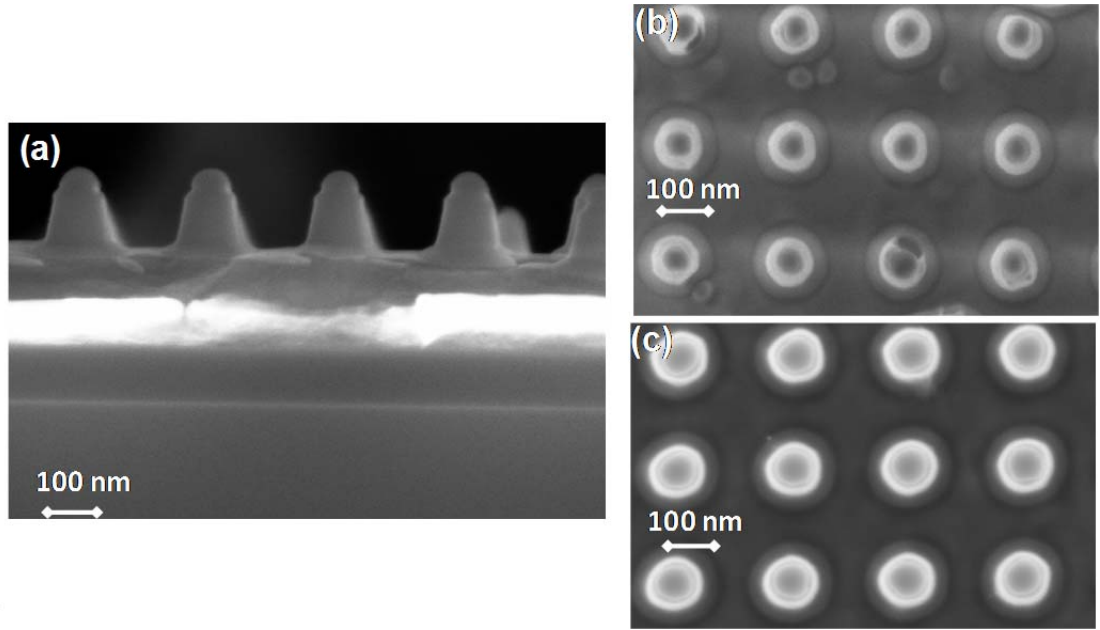present in evaporated aluminum metal.[4]

Figure 3. A. Scanning electron micrograph (SEM) cross-section of sputtered aluminum nanocone samples. B. Top-down SEM of evaporated aluminum sample. C. Top-down SEM of sputtered aluminum sample.

Optical Characterization

The subtle differences in geometry and array quality between the sputtered and the evaporated

nanostructures (

Figure **3**) lead to large differences in optical response. The normal reflectance spectra from the two

arrays (Figure 4) show two major dips: a deep resonance in the visible part of the spectrum that appears

at 610 nm for the sputtered sample and at 500 nm for the evaporated samples and multiple dips below

300 nm for both samples. The shoulders in both spectra near 825 nm are caused by (200) bulk Al

interband transitions.[4] The maximum reflectance level between the two dips near 400 nm reaches 70%

in the sputtered sample, but only 55% in the evaporated sample, indicating the presence of an additional

absorption mechanisms in that region. These differences in optical signature are due to both the

difference in material properties of the nanocones as well as changes in the cone dimensions and aspect

ratio, as shown below. In order to properly interpret the optical response of our nanostructured arrays,

we extracted average array dimensions using spectroscopic ellipsometric scatterometry.[47] In this

technique, experimentally obtained ellipsometric data are matched against a computationally-generated

library of ellipsometric signatures for a number of variations of dimensional parameters. (Details of the

extraction procedure are given in the Supporting Information). Three parameters were varied to obtain

agreement with the experimental data: height of the cones, base dimension of the cones and the

thickness of the dielectric spacer layer. Excellent agreement between the library data and the

experimental data was obtained (Figure S2, supporting information). The extracted dielectric spacer thickness was 15 nm for the sputtered arrays and 18 nm for the evaporated arrays. For the evaporated array, the extracted base of the cone was 95 nm and the cone height was 100 nm, resulting in a sidewall slope angle of 85°. For the sputtered array, the extracted base of the cone was 115 nm and the cone height 90 nm, leading to a sidewall slope angle of 77°. Such subtle changes in dimensions would be difficult to determine from electron micrograph inspection of
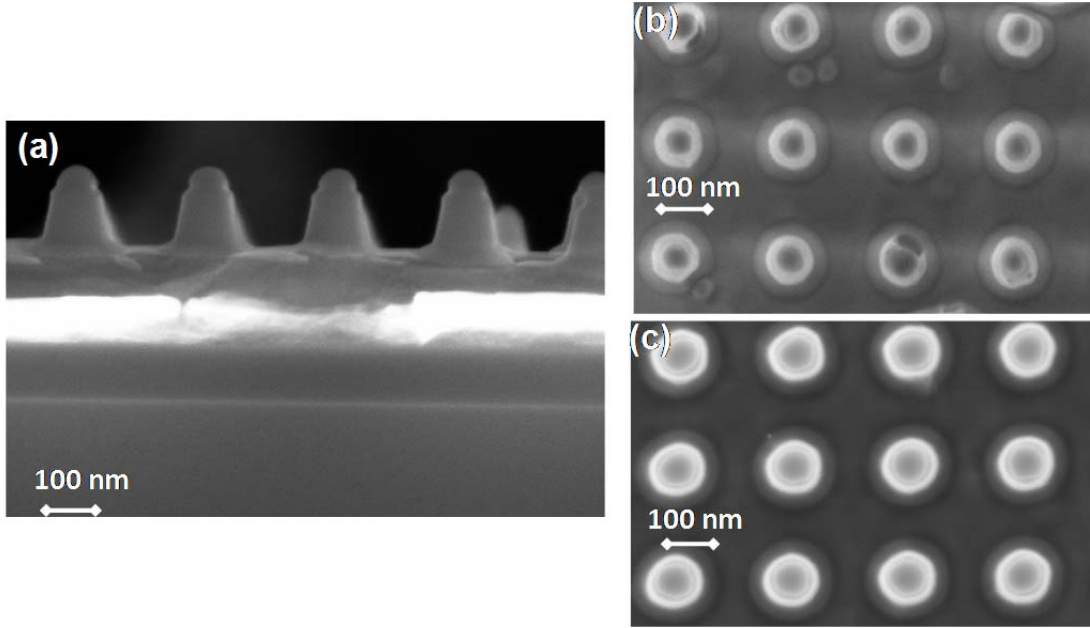

Figure **3**. Moreover, the optical measurements average structure dimensions over the ellipsometer spot size of ≈0.5 mm, corresponding to >10^3 periods. Such spatial averaging would not be possible with SEM imaging.
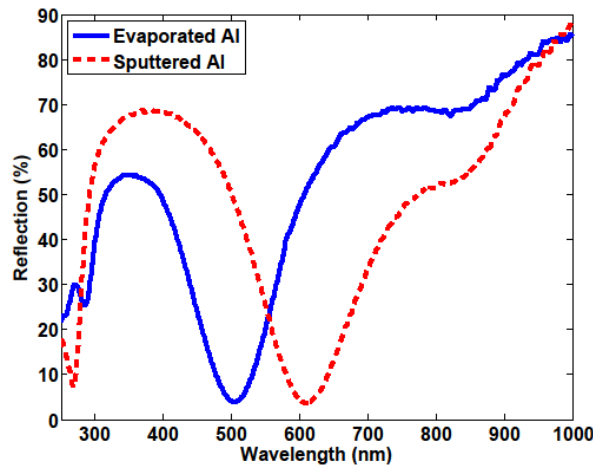
Figure 4. Normal incidence reflectance spectra from the sputtered array (dotted red line) and evaporated array (slolid blue line).

In order to assess the quality of plasmonics resonances and fully interpret the band structure, a more complete optical characterization is required in addition to normal incidence reflectance. For a broadband, broad-angle polarization-dependent analysis of the plasmonic resonances, we performed spectroscopic ellipsometry measurements of the two arrays (see Methods). The irradiation geometry and the angle of incidence for s- and p-polarizations are shown in Figure 5.
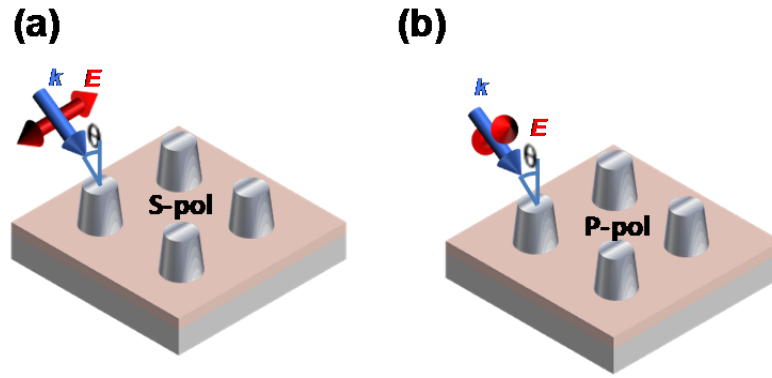

Figure 5. Geometry of the incident irradiation of the nanoplasmonic array. A. S-polarization. B. P-polarization.
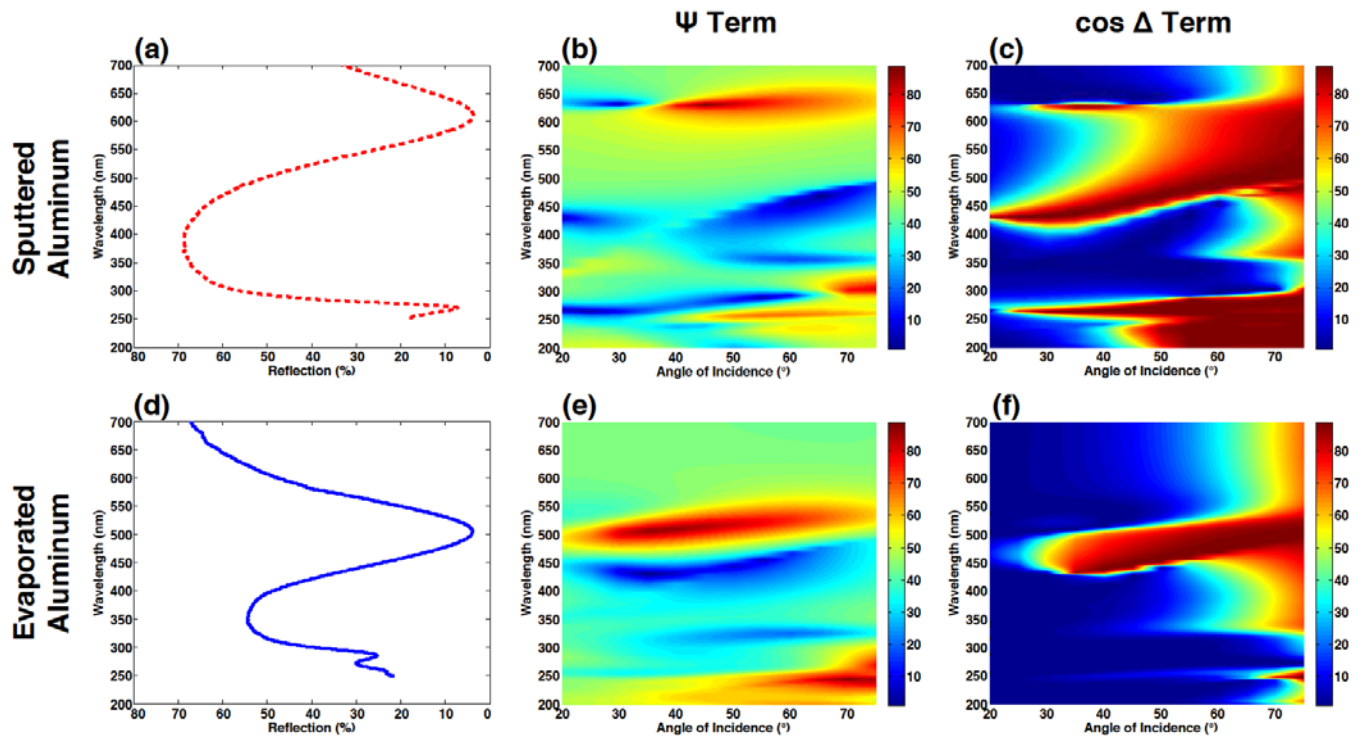
Figure 6. Normal-incidence reflectance, Ψ ellipsometric parameter and $cos(\Delta)$ ellipsometric paramater for sputtered samples (A, B, C, respectively) and evaporated samples (D, E and F, respectively).
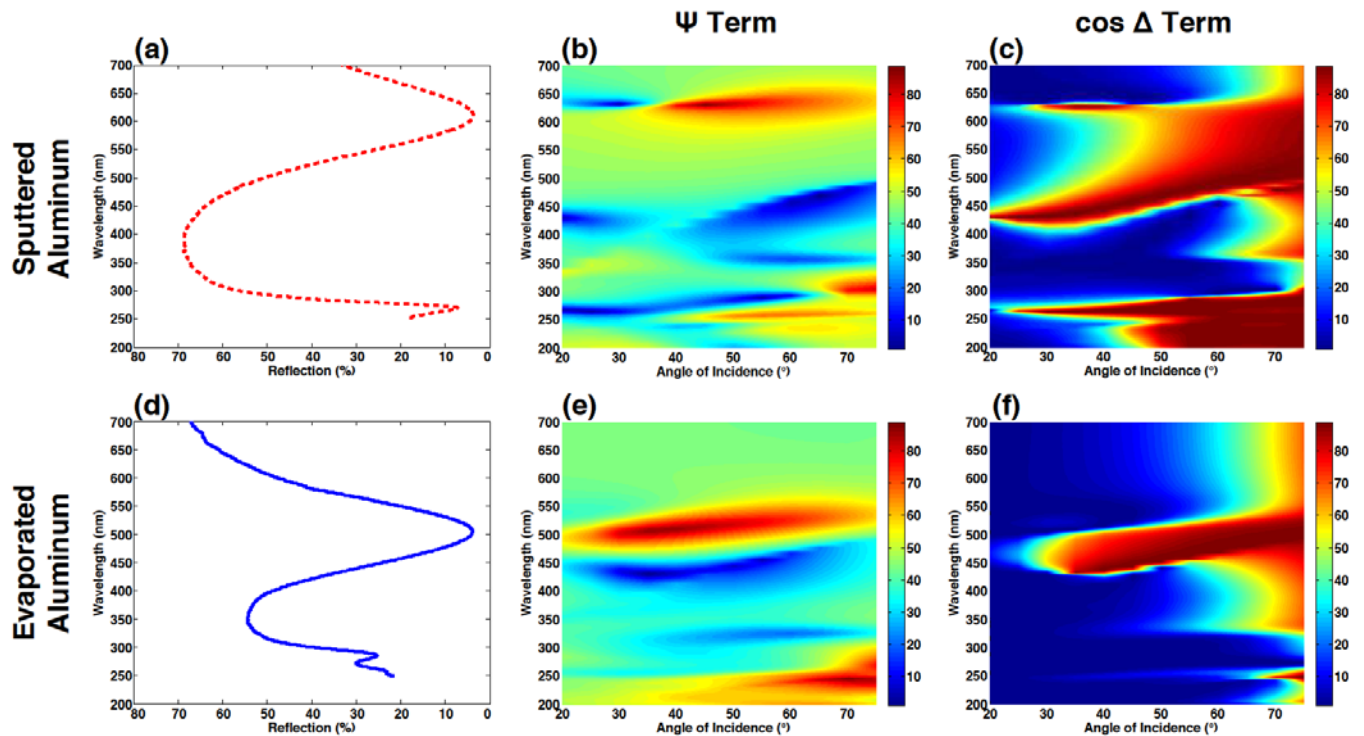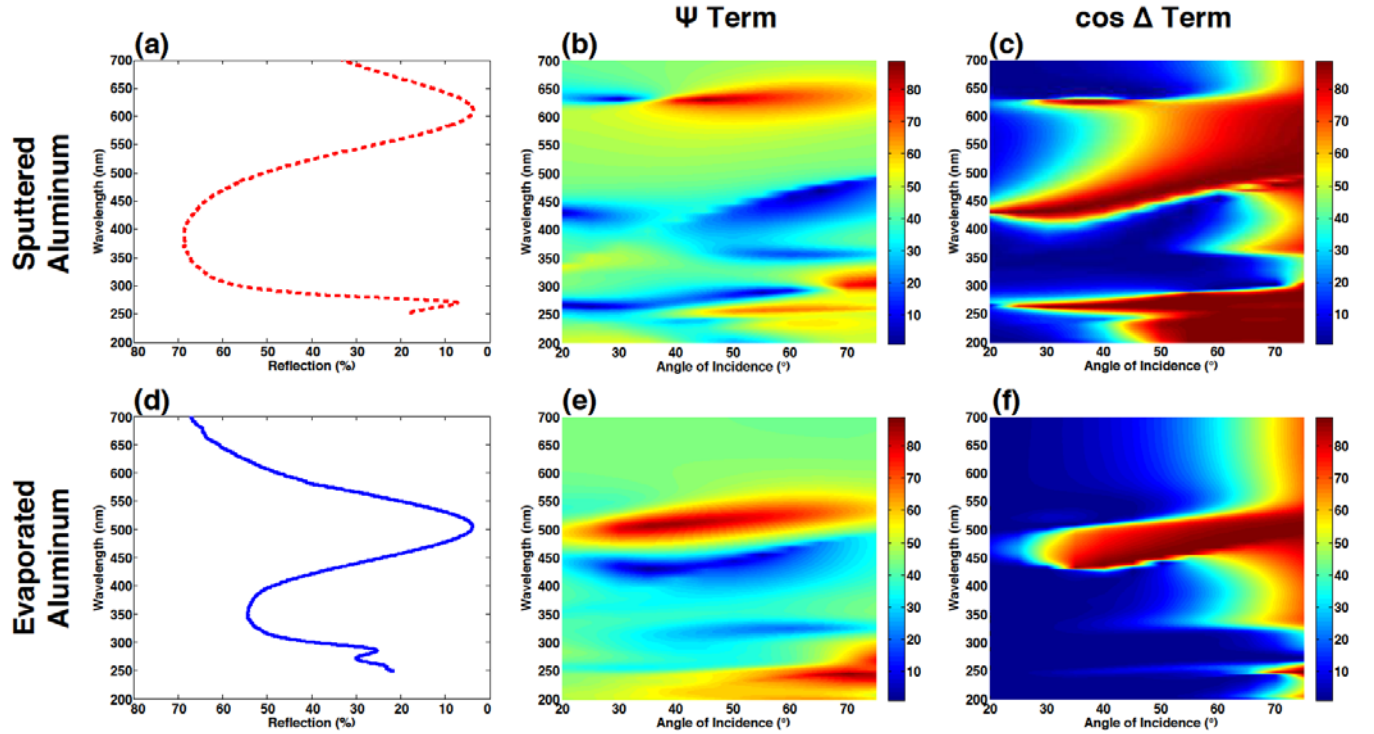

Figure **6** compares previously-shown reflectance data for the sputtered and evaporated arrays (

12

Figure **6**A and D, respectively) with the spectroscopic ellipsometry data for the same arrays (

Figure **6**B, C for sputtered and E, F for the evaporated). The ellipsometric parameter Ψ represents the

ratio of complex reflectances r_s and r_p at two polarizations and Δ represents the phase between these two

reflectances,
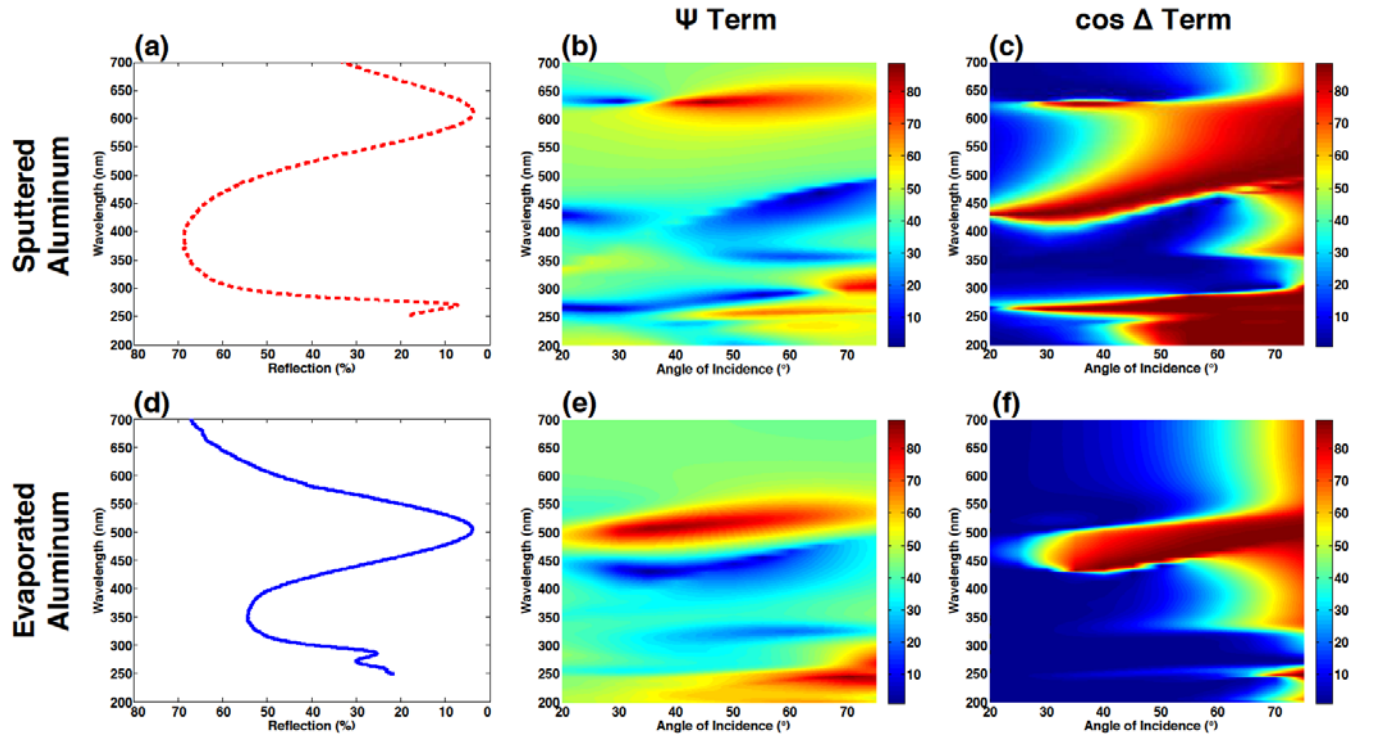
$$\rho = \frac{r_p}{r_s} = \tan(\psi)e^{i\Delta} \tag{1}$$

The data in

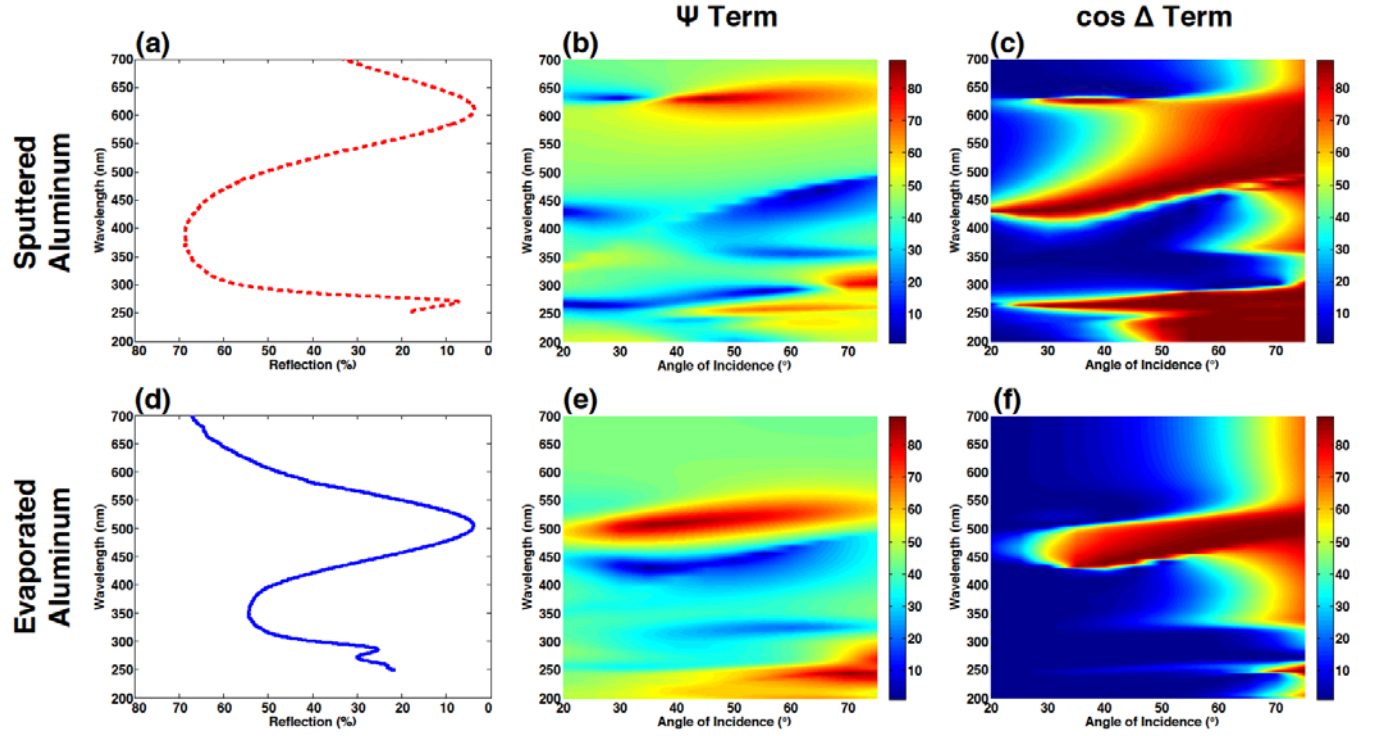Figure **6**B and E are a representation of the plasmonic band diagram, as mapped out by spectroscopic ellipsometry. The wavelength vs. angle-of-incidence (AOI) map could have been re-cast as the more conventional ω vs. k diagram, but due to the uniform point density along the angle-of-incidence axis, the representation in
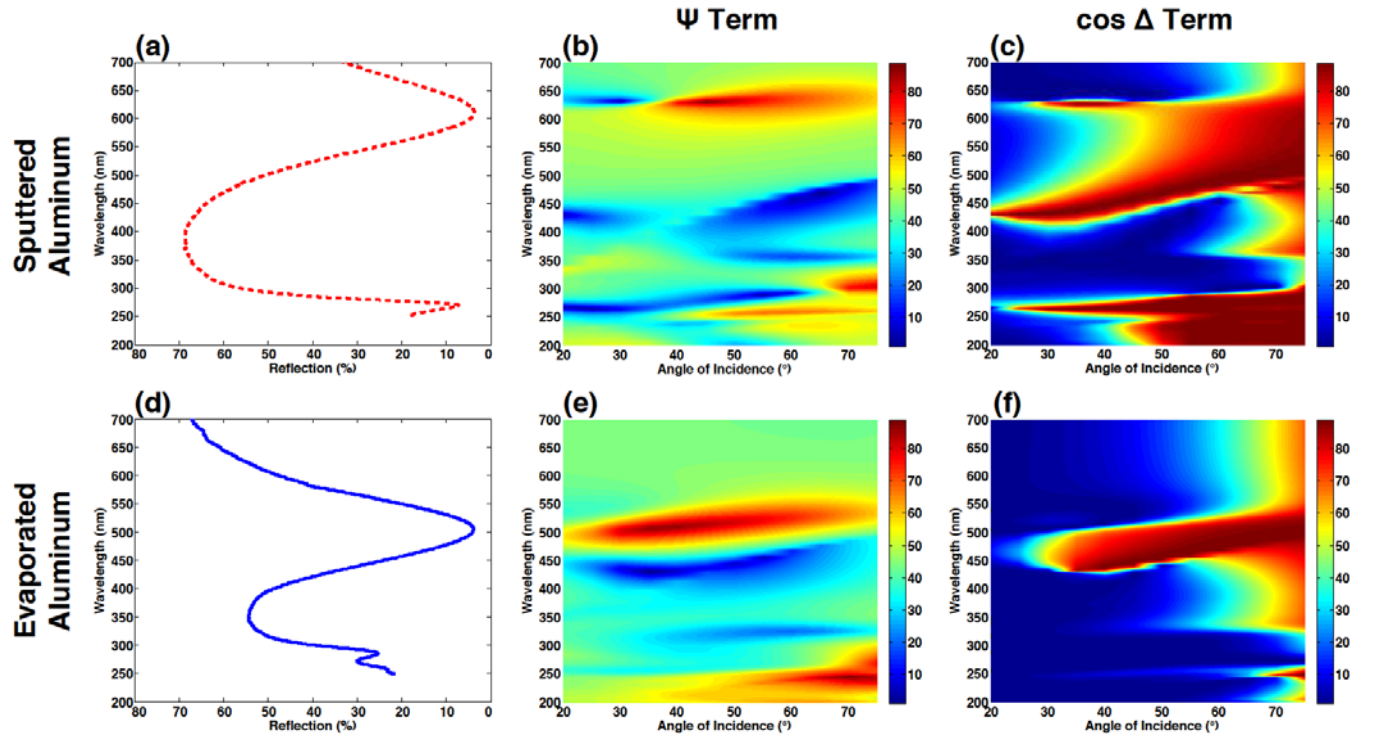
Figure **6** is more appropriate.[42] In equation (1), when the condition for the *s*-resonance is met, the

magnitude of the right-hand side becomes large as Ψ tends to 90°. Thus, bright red colors in
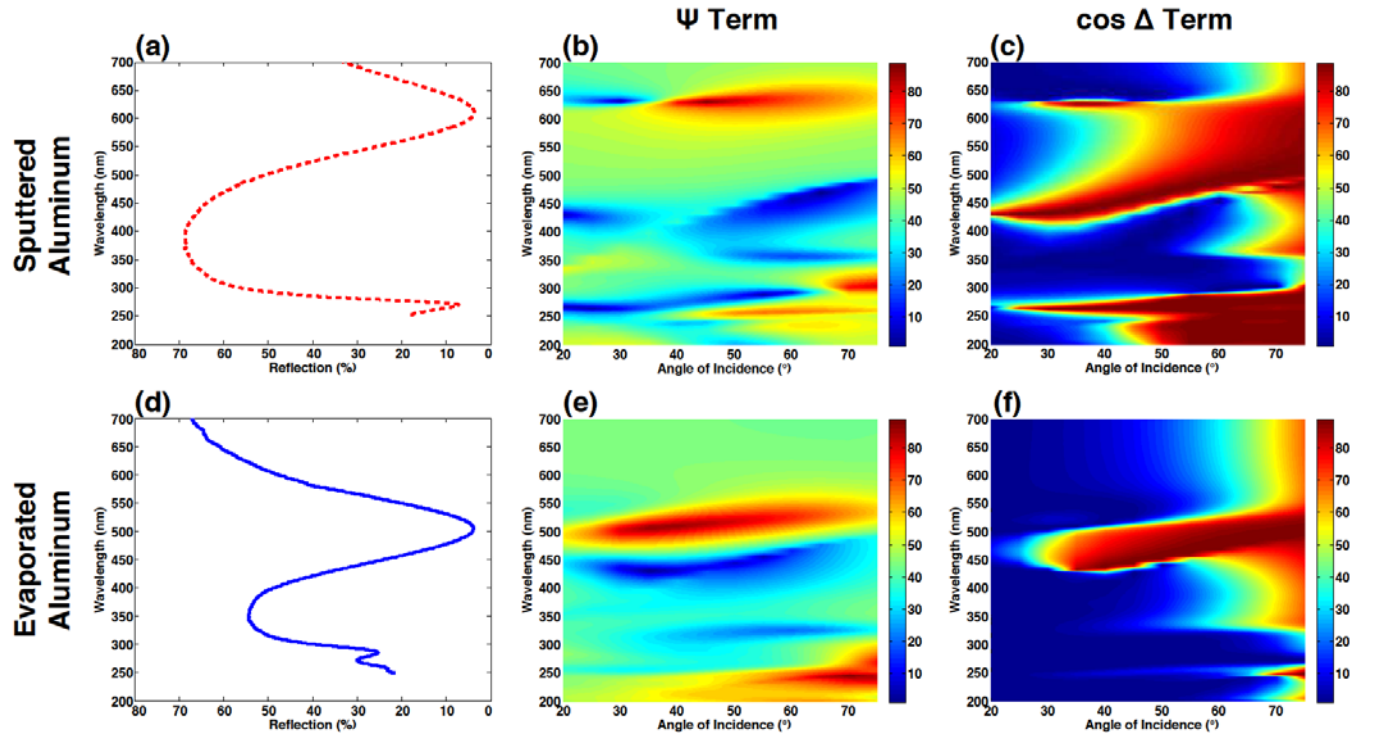

Figure **6**B and E represent *s*-resonances. Analogously, dark blue colors in
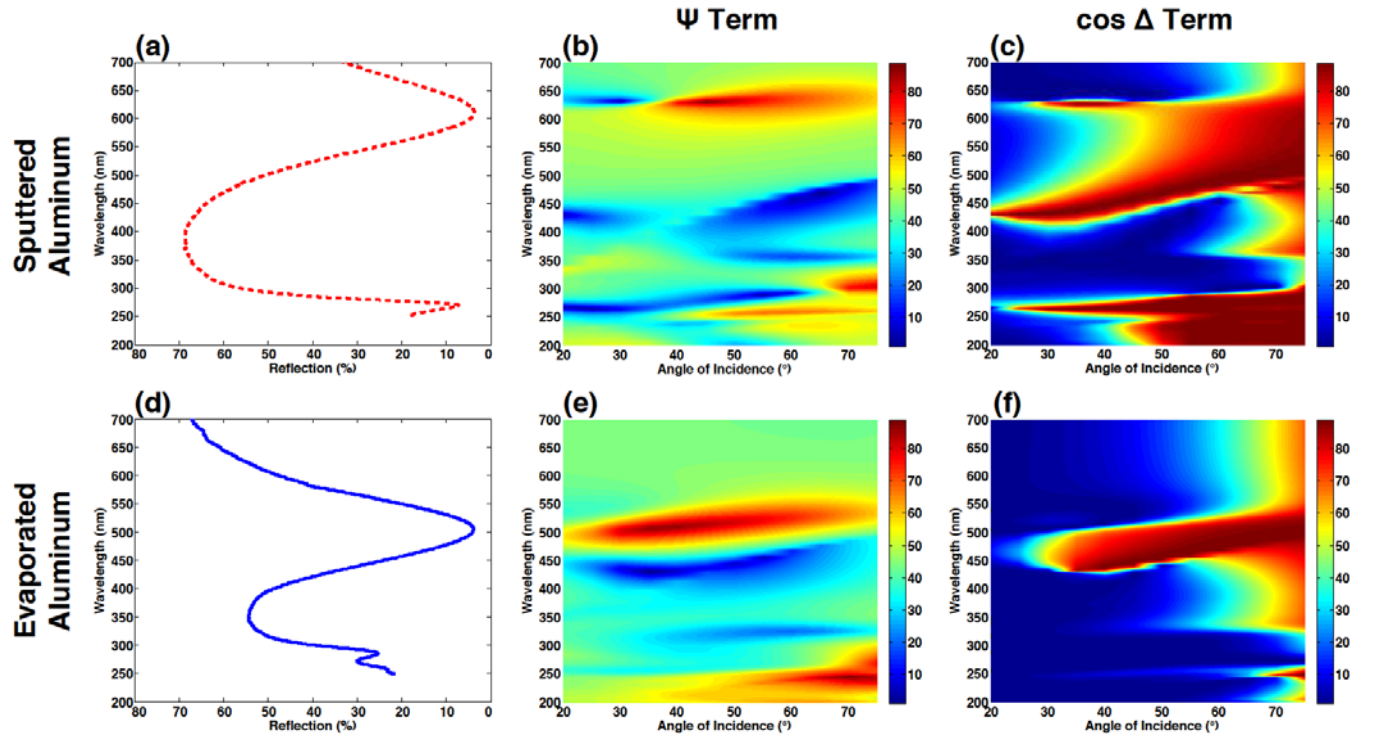
Figure **6**B and E represent *p*-resonances. As observed by others, the location of these plasmonic resonances is accompanied by a sharp change in phase (
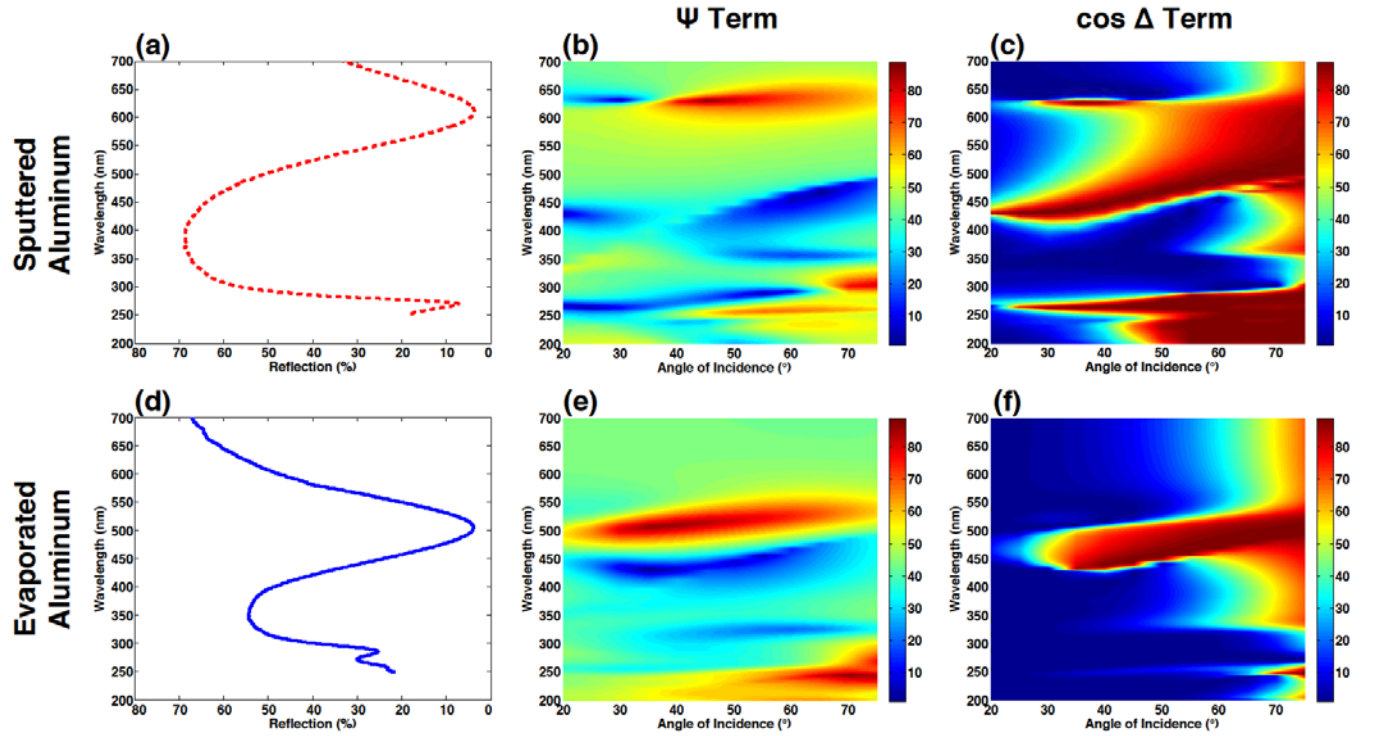

Figure **6** C and F).[48]
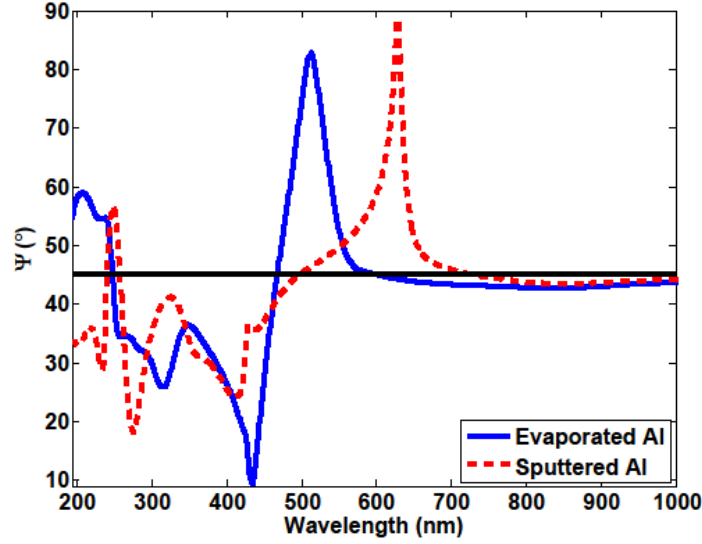
Figure 7. Ellipsometric Ψ parameter vs. wavelength for 45 degree incident angle for evaporated (dashed blue) and sputtered (solid red) samples

From the correspondence to the normal incidence reflectance data, the angle-independent modes at 620 nm for the sputtered sample and 500 nm for the evaporated sample are identified with the primary LSP resonance modes. These excitations can be recognized as a magnetic dipole resonance, which arises from the coupling between the bottom of the plasmonic pillar and the top of the metal underlayer to form a localized current loop.[49]   The electric field distribution for these localized modes is strongly confined at the lower edge of the aluminum cones and thus is highly sensitive to material losses. Comparing the width of this LSP resonance between the two samples, we observe a much sharper resonance in the sputtered sample. This difference is highlighted by examining the Ψ parameter as a

function of wavelength for a 45° angle of incidence (
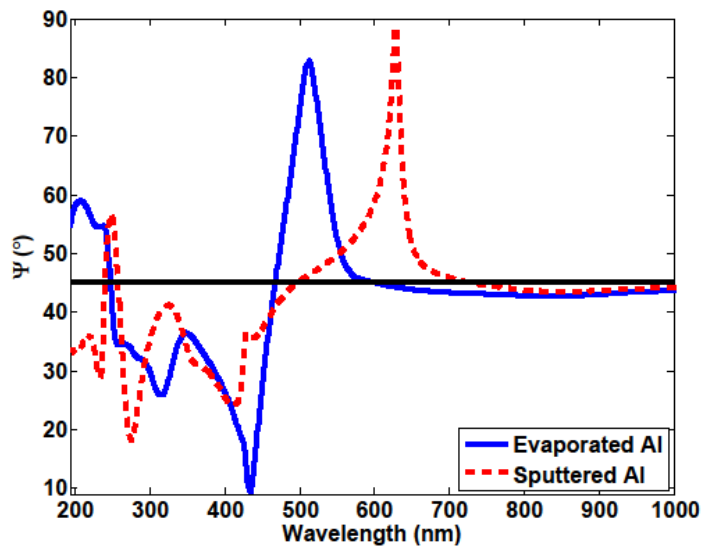
Figure **7**). The narrower plasmonic linewidth of the LSP resonance for the sputtered sample can be due to at least two reasons. First, since the position of plasmonic resonance is sensitive to cone dimensions, better uniformity of the sputtered Al plasmonic cones (
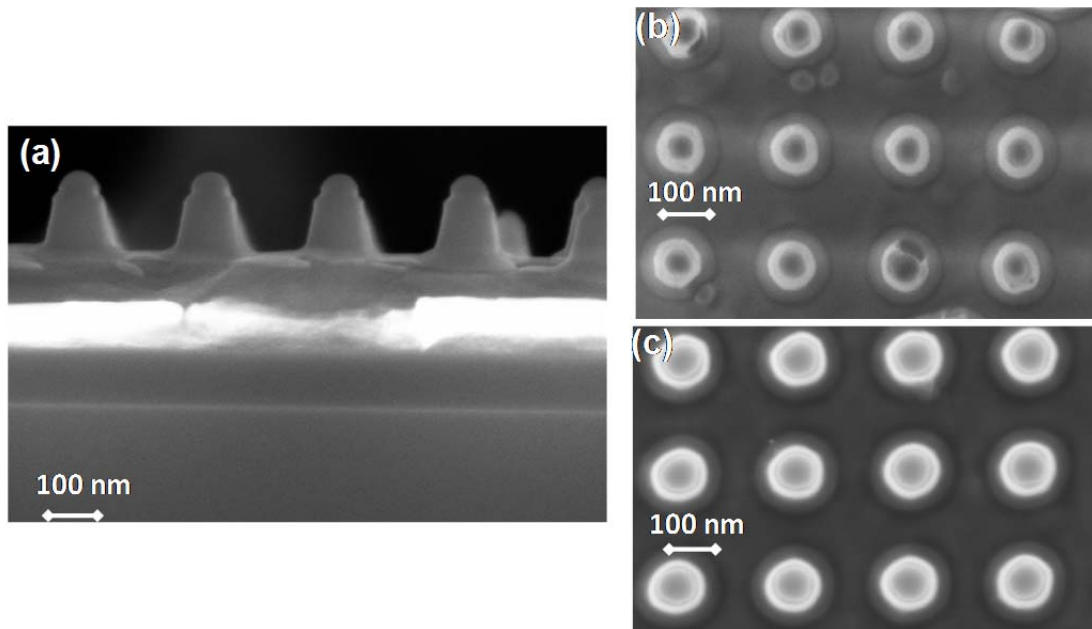
Figure **3** B vs. C) can lead to narrower linewidths. Second, higher quality sputtered aluminum leads to a higher quality factor of the resonance, resulting in a sharper peak.

It is instructive to note that, although oblique angle-of-incidence data show a substantial difference between the widths of the plasmonic resonance (
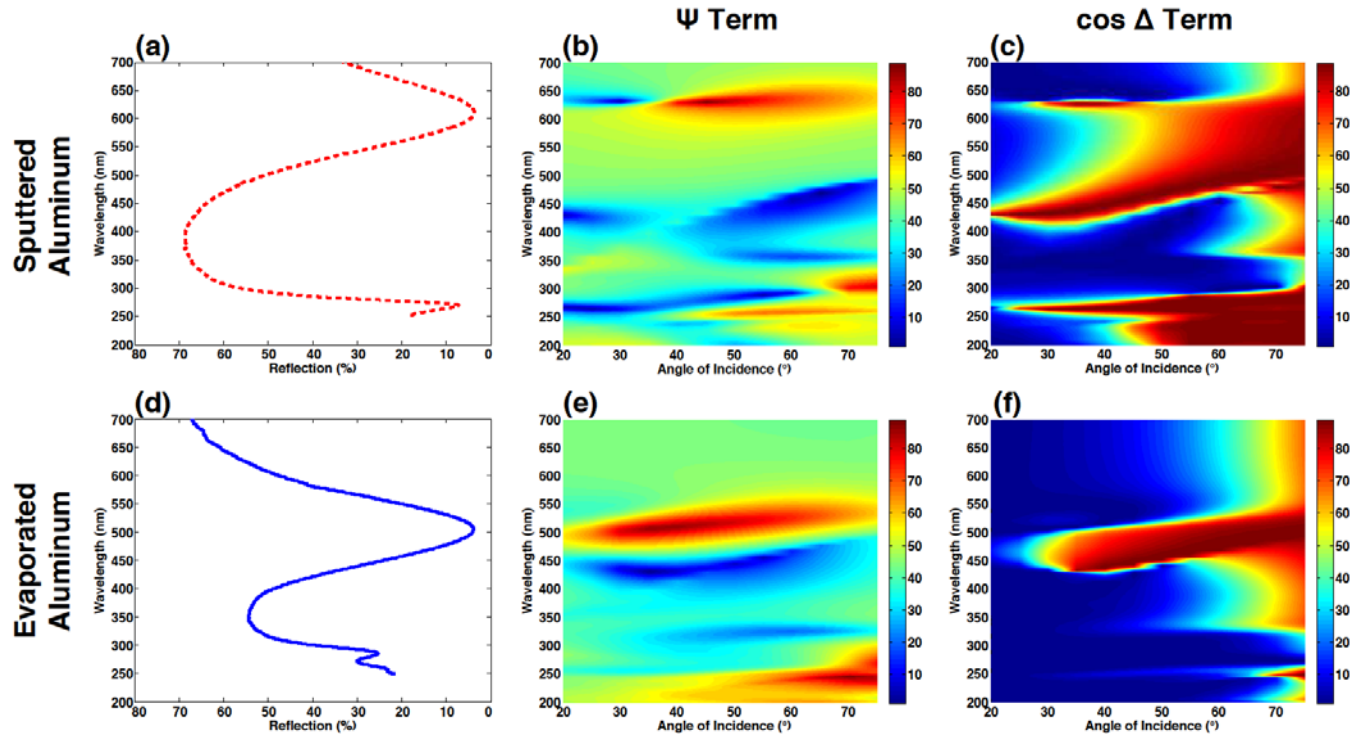
Figure 6 B vs. E), the normal-incidence data for the two arrays show comparable linewidths (
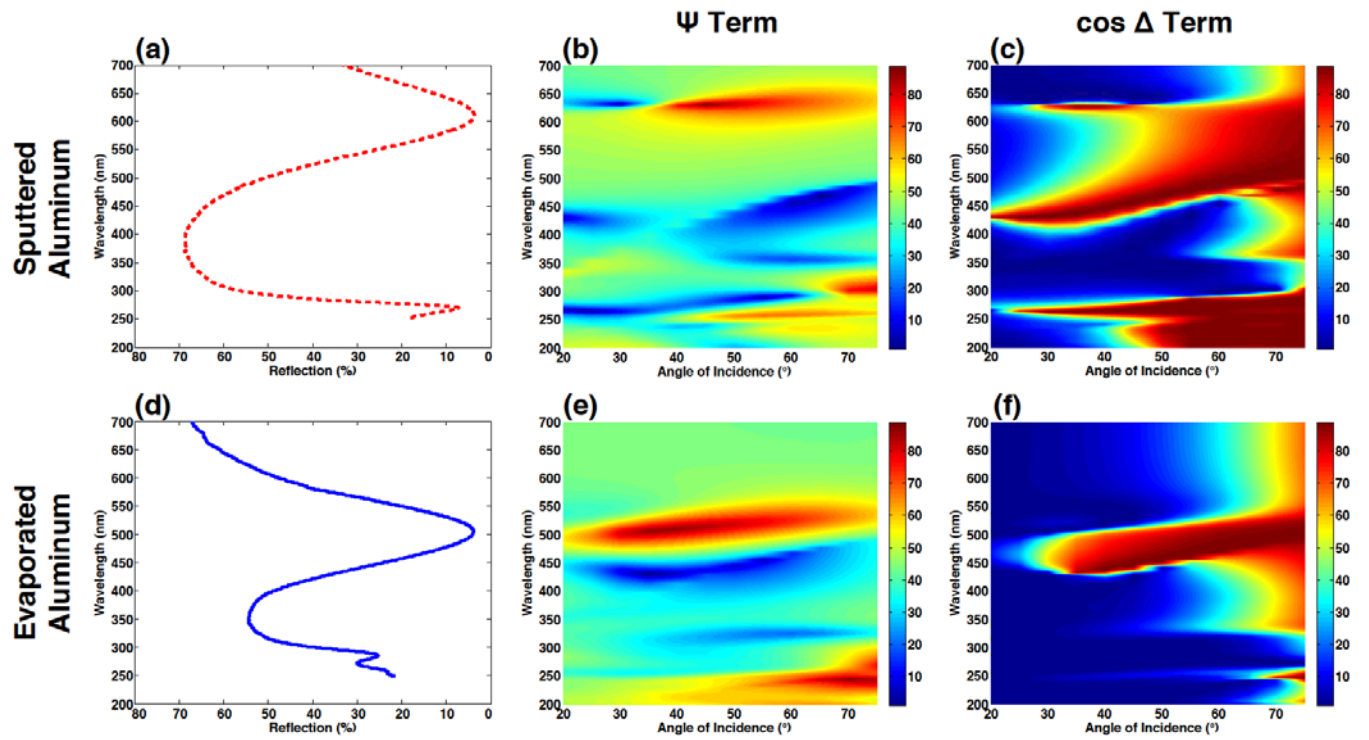
Figure **6**A vs. D). The difference between the normal-incidence and the oblique-incidence data is investigated by examination of near-field profiles for 0 vs. 45 degrees angle of incidence at 620 nm (
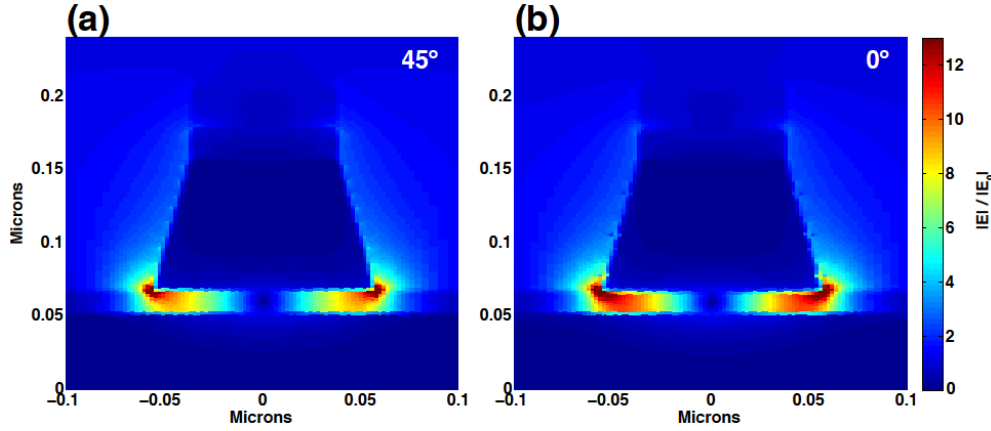
Figure **8**). At 45 degree AOI, the electric field intensity is highly localized at the edge of the


nanocones (
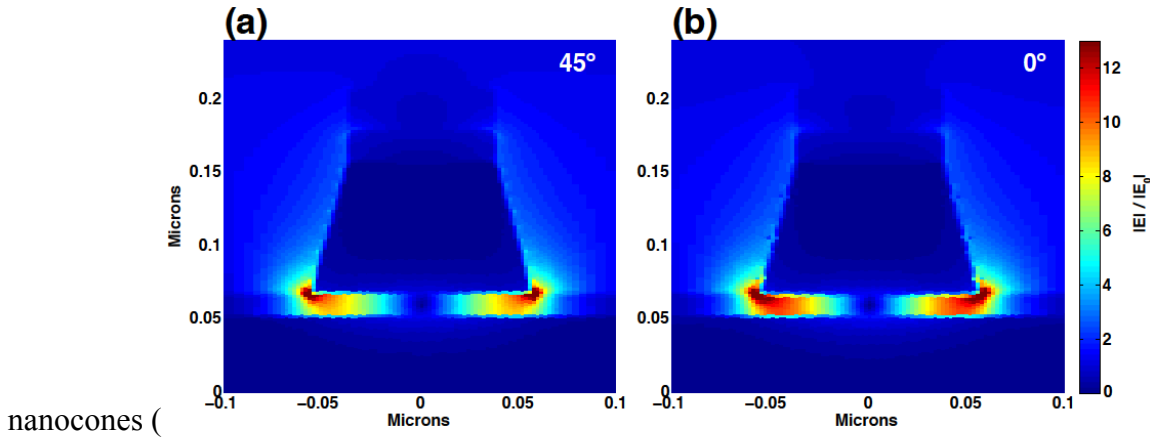
Figure **8**A), whereas at the normal incidence, the interaction with the aluminum underlayer is

considerably greater (
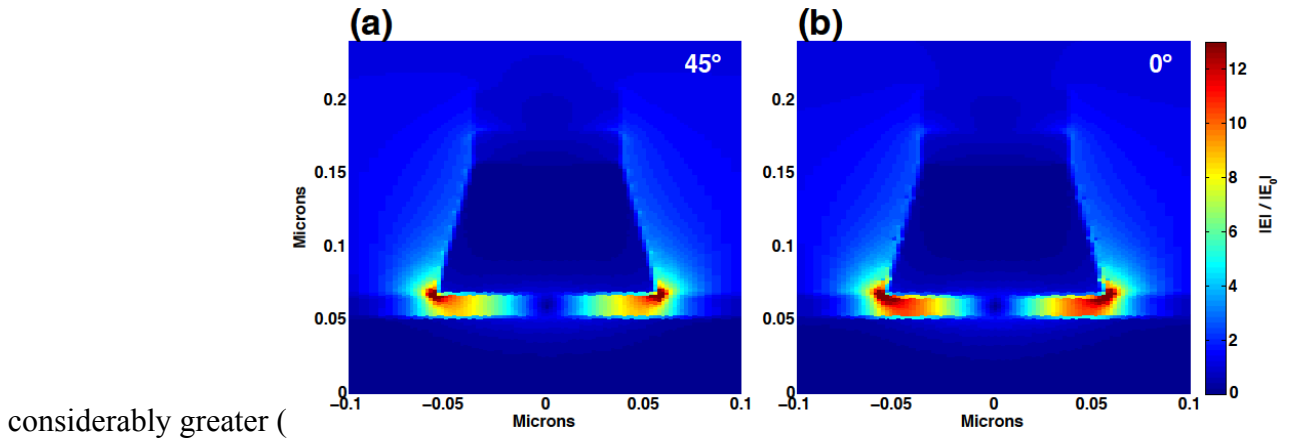
Figure **8**B). Since for both our structures the aluminum underlayer is prepared from unoptimized aluminum, resonance broadening at 0° over 45° incidence angle can be expected due to larger scattering

from the aluminum underlayer.[4] Thus, the oblique angle-of-incidence data represent a more accurate assessment of the plasmonic resonance quality in the nanocones.
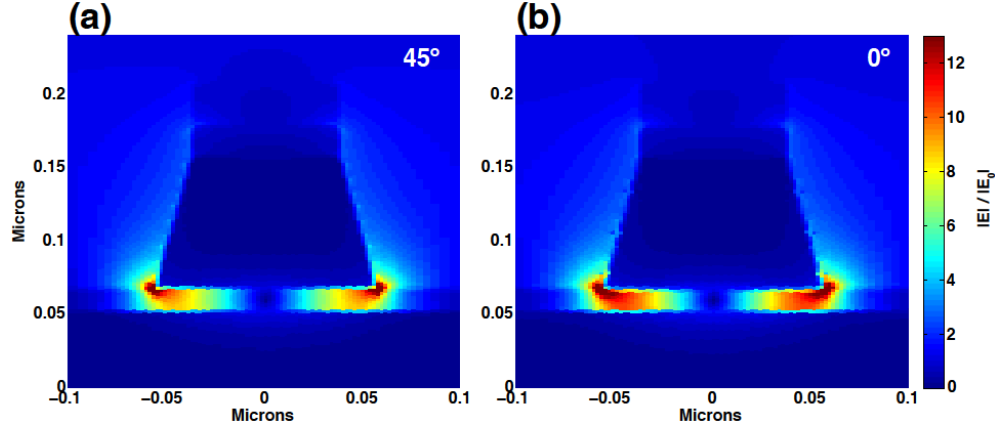
Figure 8. Cross-section field profiles for the sputtered aluminum sample at 45° incident angle (A) and 0° incident angle (B) at 620 nm.

Identification of the rest of the modes on the plasmonic band diagram of
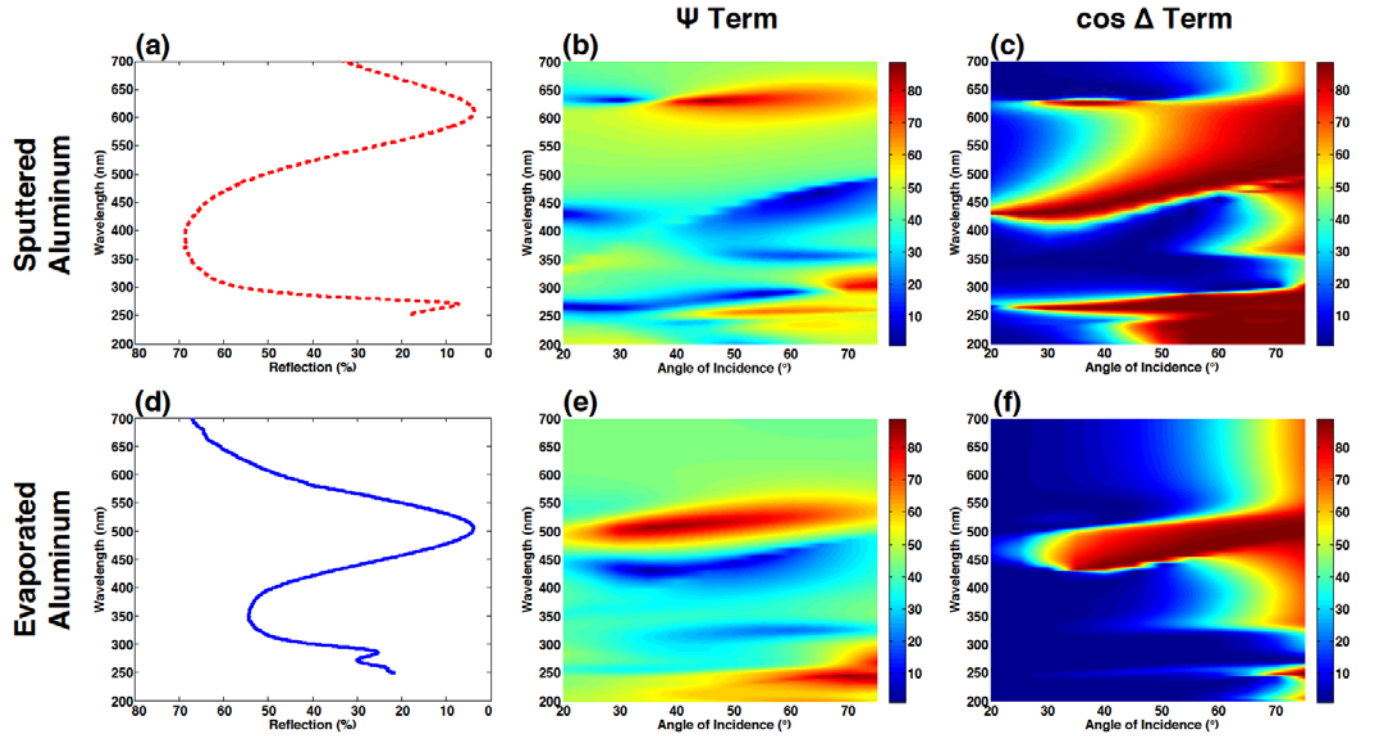
Figure **6** is complicated by the cone taper in the structure and the strong coupling between various modes. However, from the dimensional extraction with ellipsometric scatterometry described above, plasmonic mode identification could be verified with full-field numerical simulations. By inspecting the appropriate field profiles, we can assign these modes as follows. The intense *p*-polarized band observed

around 470 nm at high angles and shifting to lower wavelength for lower angles is caused by the vertical resonance within the nanocones. The *p*-polarized resonance around 350 nm in the sputtered sample and at 320 nm in the evaporated sample is due to the higher-order (quadrupolar) resonance localized at the bottom of the structure. The reflectance curves (Figure 4) do not show sharp resonances between 300 and 500 nm, but a broader depression in reflection suggests broadened overlapping resonances in that region. The strong *p*-band observed between 250 and 300 nm (
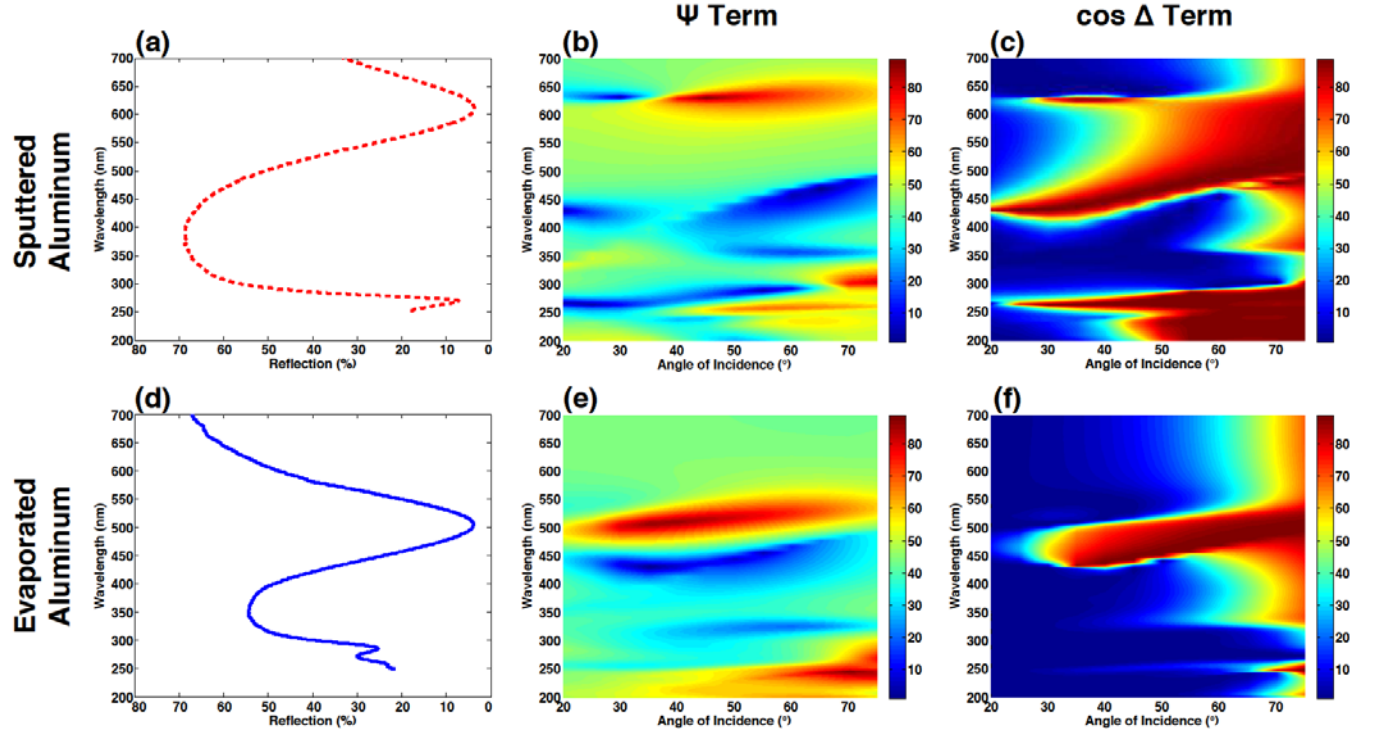
Figure 6B) results from a gap mode (see discussion below and
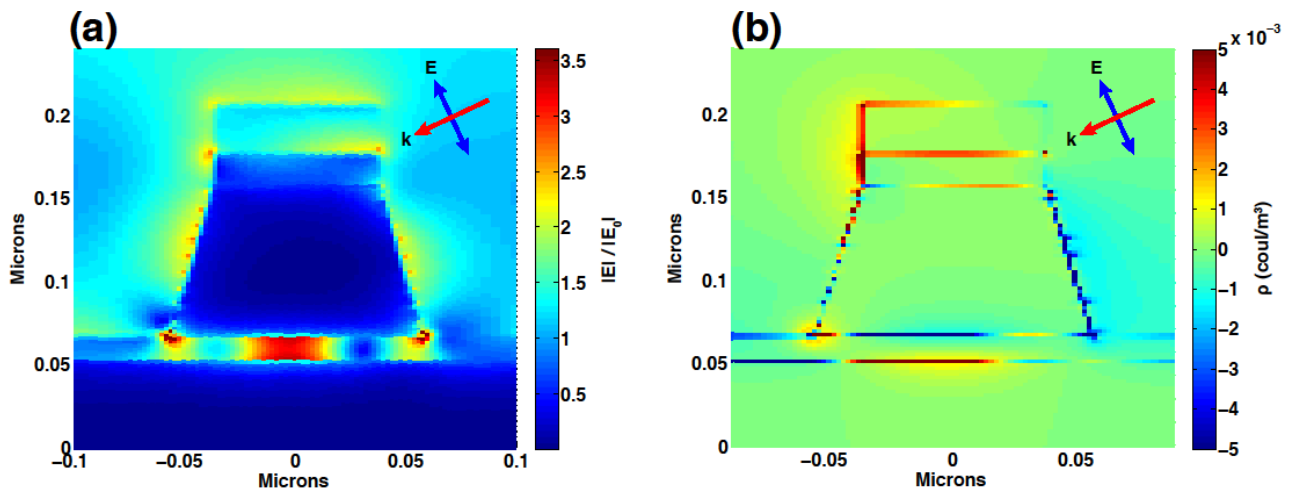
Figure **10**). Additional bands observed below 250 nm both in reflectance and in ellipsometric data involve coupling with various SPP bands, as predicted by plasmon dispersion curves (Supporting information, Figure S3).

As a final part of the study, we have extracted the depolarization parameter from the ellipsometric data acquired along the high symmetry directions. For isotropic samples, depolarization can be described as a mixture of a non-depolarizing matrix and an ideal depolarizer. The degree of polarization, *p*, is extracted from the isotropic ellipsometry parameters, *N*, *C* and *S*,[50] where:

$$p = \sqrt{N^2 + C^2 + S^2} \tag{2}$$

In the above, *N= cos (2 Ψ)*, *S = sin(2 Ψ)sin(Δ)*, and *C = sin(2 Ψ)cos(Δ)*, where *Ψ* and Δ are the traditional ellipsometry angles. The % depolarization is then defined as

$$\%depol = 100 \times (1\text{-}p^2) \tag{3}$$

In our case, the high symmetry array directions were identified by performing azimuthal in-plane scans and identifying the angles where the off-diagonal Mueller matrix elements were minimized (see Methods).
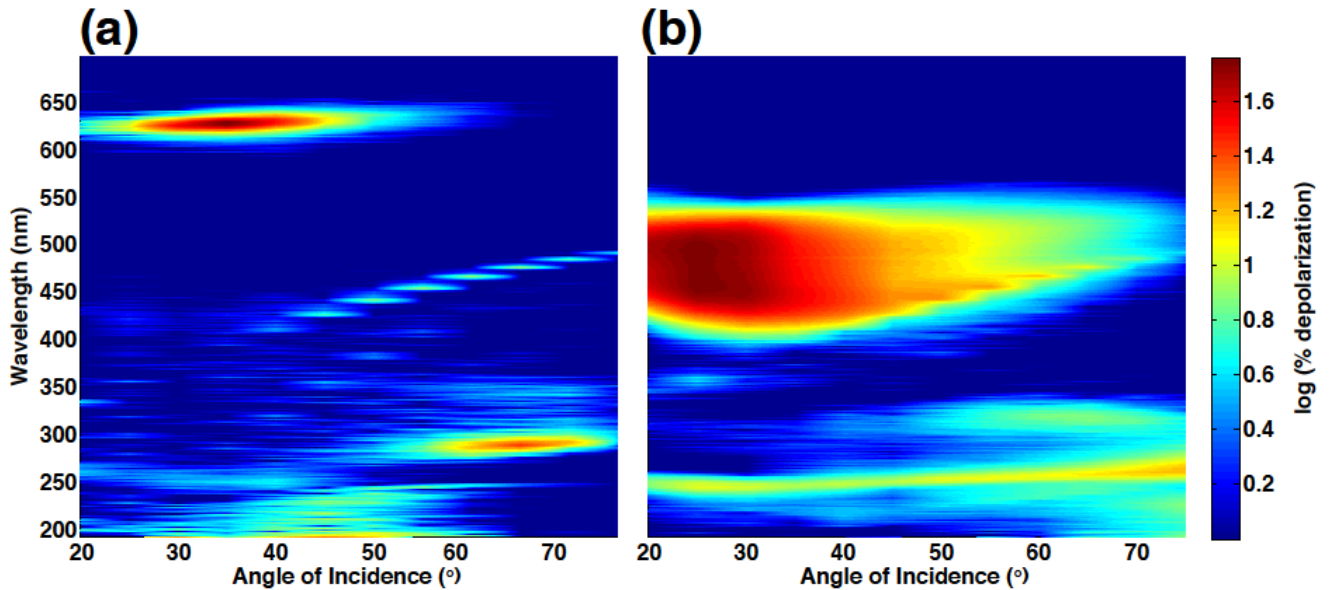
Figure 9. Ellipsometrically acquired spectral depolarization map for the sputtered sample (A) and evaporated sample (B).

The highest depolarization for either sample (

Figure **9**) occurs at the spectral position of the main plasmonic resonances (see
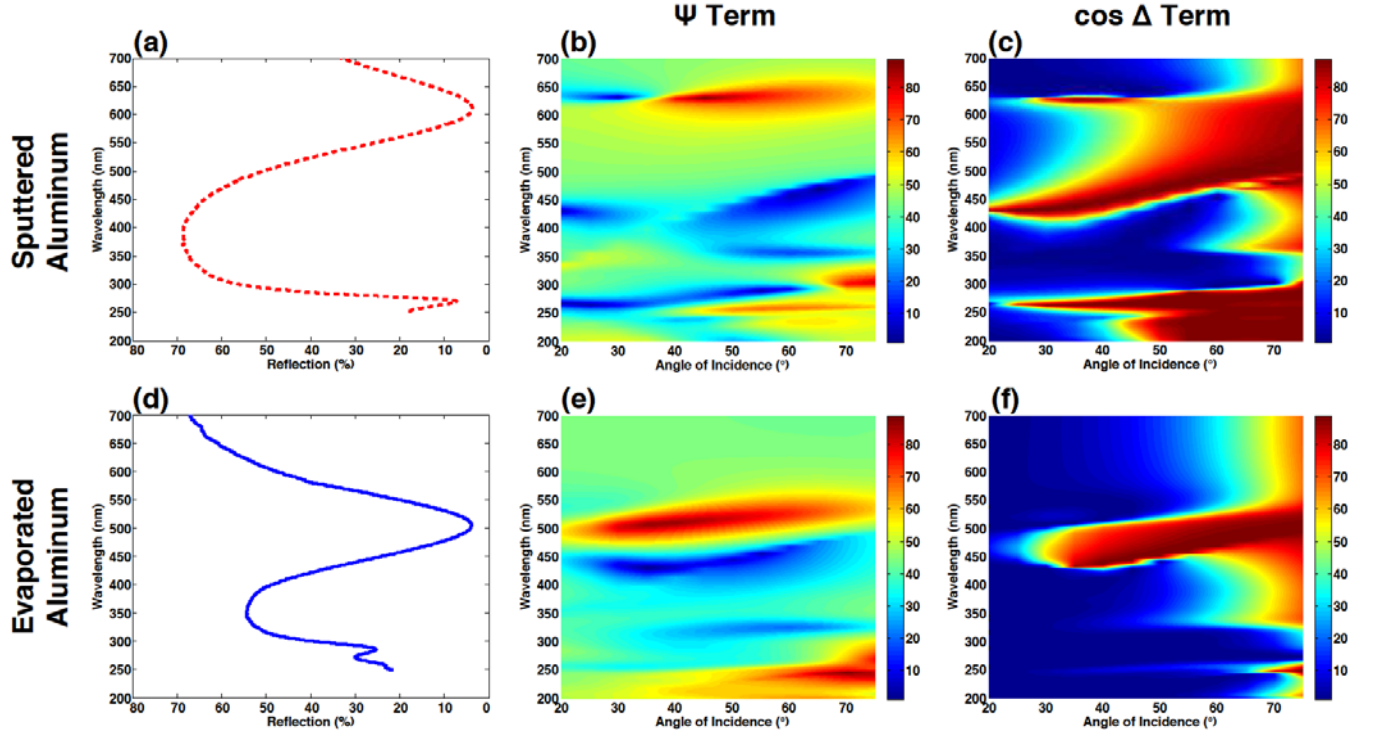
Figure **6**), where depolarization for both samples reaches nearly 70%. By contrast, no depolarization is observed in the spectral regions away from plasmonic resonances. The spectral bandwidth of maximum depolarization for the evaporated sample (

Figure **9**B) is much broader than that of the sputtered sample.

Previous work on diffractively coupled plasmonic dimer arrays similarly measured the spectral regions of maximum depolarization utilizing spectroscopic ellipsometry.[51] That work demonstrated that maximum depolarization occurred in the regions of the maximum electric field enhancement. The authors postulated that depolarization arose due to the finite detector size which was able to capture a finite range of diffracted wavevectors, each characterized by a well-defined polarization state. In the vicinity of the plasmonic resonances, the higher spatial near-field localization directly translated to the increased depolarization in the far field due to the larger angular spread of the wavevectors.

In this work, we further suggest that the narrow spectral bandwidth of the depolarization for the sputtered sample arises from the higher resonance quality of that sample. By comparison, the broader spectral bandwidth of the depolarization for the evaporated sample arises from the broader spectral width of that resonance (
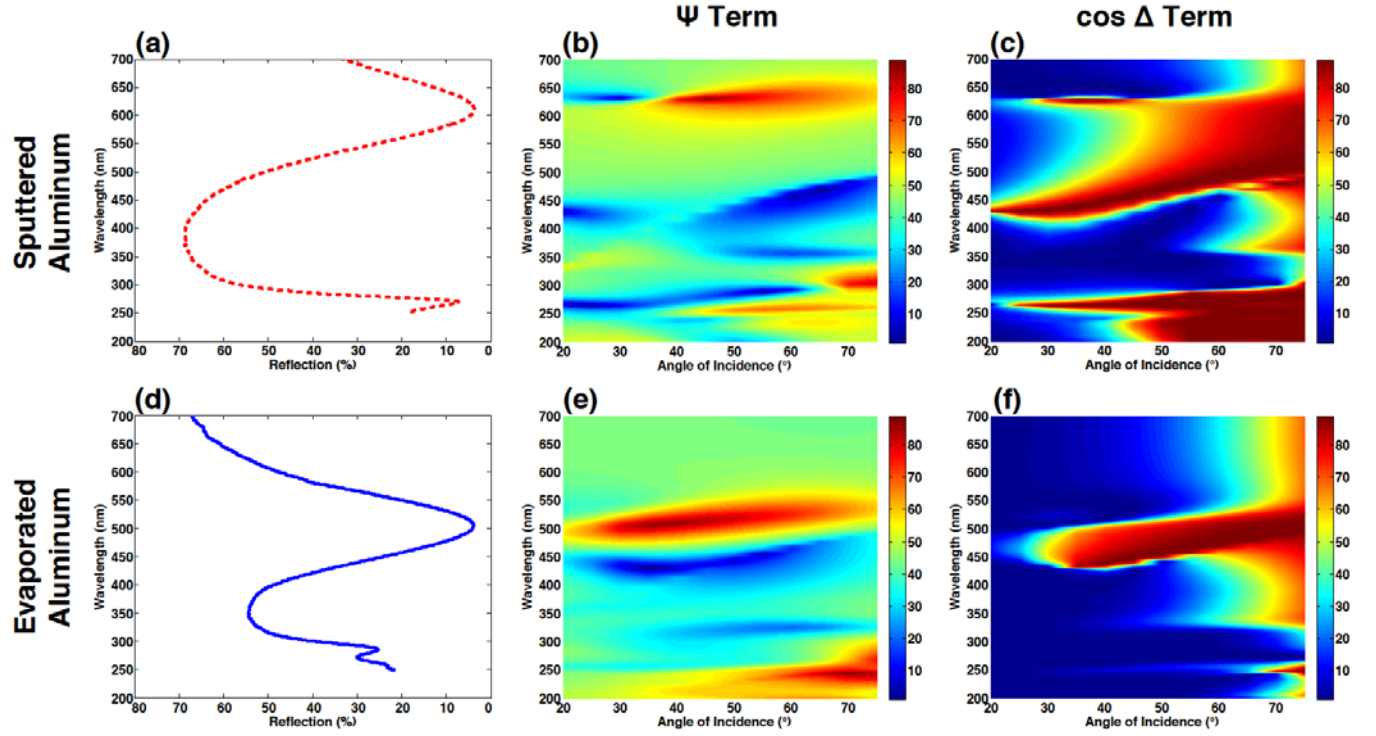
Figure **6**E).

It is also interesting to observe a second, high depolarization region occurring in both samples at higher angles of incidence between 250 and 300 nm. Near-field and the charge density simulations for this mode suggest strong field localization at the bottom of the structure, with additional coupling across

the dielectric gap into an SPP mode in the underlying metal (See
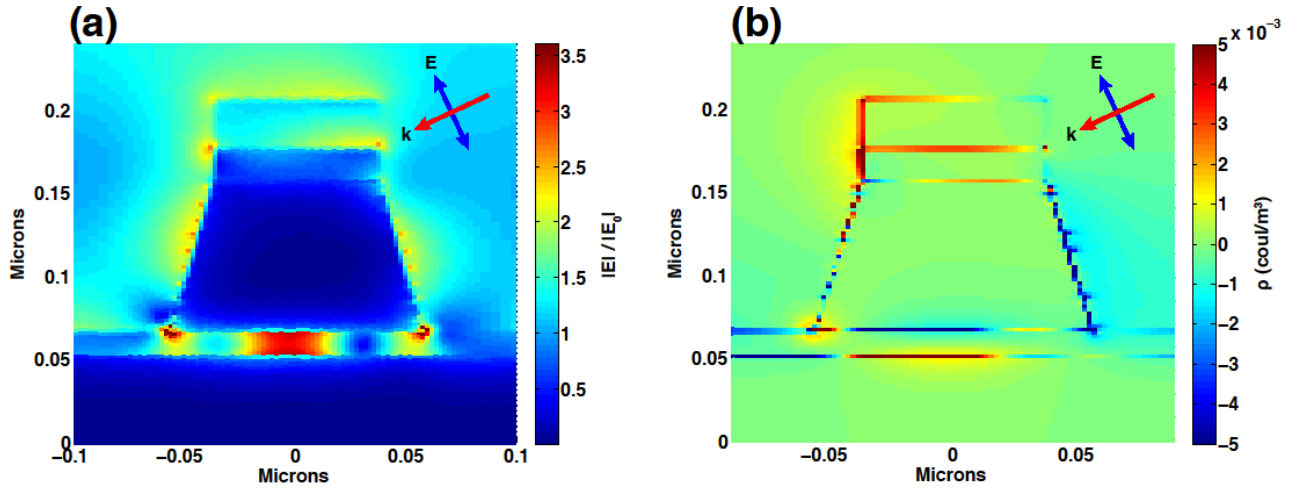
Figure **10** A and B). Once again, we suggest that the strong field localization is observed in the far-field as an increase in the depolarization parameter.
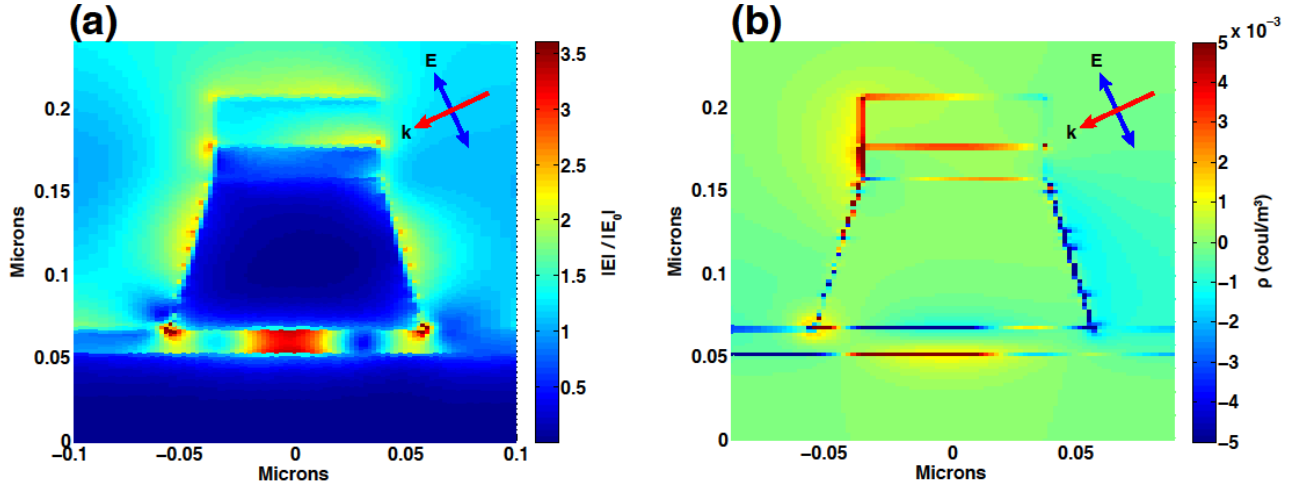
Figure 10 Cross-sectional field profile (A) and charge density (B) for the sputtered sample, calculated from full-field simulations at 65° angle of incidence. The upper-right inset on each plot shows the geometry of the incident *k*-vector and the electric field.

CONCLUSIONS

We have developed a robust, wafer-scale fabrication method for aluminum nanoplasmonic structures for ultraviolet and visible applications. Two sets of structures, utilizing conventional evaporated aluminum and improved high-temperature-sputtered-and-polished aluminum, were fabricated and characterized utilizing spectroscopic ellipsometry. The differences in thin film processing lead to different grain structures and slightly different nanostructures dimensions. Although these differences

appear to be small as observed by conventional scanning electron beam imaging, they nevertheless have a profound effect on the near-field and far-field optical behavior of plasmonic resonators. Significantly higher quality resonances were demonstrated for the nanostructures fabricated using the improved aluminum deposition process. Furthermore, depolarization data obtained with spectroscopic ellipsometry suggests that structures fabricated in the improved aluminum exhibit better near-field spatial localization when compared with evaporated aluminum films. This fabrication demonstration provides a robust platform for CMOS-compatible, wafer-scale plasmonic devices that enable a range of efficient sensing and light-harvesting applications in the ultraviolet-to-visible wavelength range.

METHODS

Simulations

For dimensional extractions utilizing the ellipsometric scatterometry method, Rigorously Coupled Wave Analysis software Unigit was used (see supporting information).[52] For full-field electromagnetic simulations, Finite Difference Time Domain Method software FDTD Solutions from Lumerical Corporation was used.[53]

Spectroscopic ellipsometry measurements

The data were acquired using a dual-rotating compensator ellipsometer (J.A. Woollam RC2®) over the wavelength range from 193 to 1690 nm at angles of incidence between 20° and 75° in steps of 5°. The sample was mounted on an automated rotation stage and data was acquired for azimuthal orientations between 0° and 360° in increments of 7.5°. Focusing probes were used to reduce the beam diameter at the measurement spot to approximately 250 μm. The entire 4x4 Mueller matrix data normalized by the element M_{11} were obtained at the above experimental conditions. For the analysis in this paper, only the data along the high-symmetry directions are presented.

Fabrication of nanopillar arrays

To fabricate both samples, 8" diameter (100) silicon was used as the starting substrate. The first layer in both samples was 200 nm thick aluminum deposited using DC magnetron sputtering in an argon-hydrogen environment. The deposition power was 1 kW, the Ar flow rate was 10 sccm, and the

90%:10% Ar:H flow rate was 15 sccm. There was no active control of the substrate temperature, and the film thickness was verified using spreading sheet resistance. The second layer in both samples was 20 nm thick aluminum oxide deposited using atomic layer deposition. For both samples, the oxide was thermally deposited at 300°C using trimethylaluminum and deionized water. The film thickness was verified using spectroscopic ellipsometry.

The third layer was the only layer that was different between the two samples. The first sample had a 500 nm thick aluminum film deposited on the aluminum oxide layer using DC magnetron sputtering in an argon environment. The deposition power was 2 kW, the Ar flow rate was 50 sccm, and the chamber pressure was 6 mTorr. The substrate was kept at 350°C during deposition, and the film thickness was verified using spreading sheet resistance. This was followed by a chemical mechanical polishing (CMP) step to thin the aluminum to ≈130 nm. The combination of high deposition temperature and CMP was used to produce an aluminum film with both large grain size and low surface roughness.[4] The second sample had a ≈130 nm thick aluminum film deposited on the aluminum oxide layer using electron beam evaporation with no active control of the substrate temperature at a base pressure of $9.5x10^{-9}$ Torr and a deposition rate of 0.5 Å/s.

The fourth layer in both samples was 20 nm thick titanium nitride deposited using DC magnetron sputtering in an argon-nitrogen environment. The deposition power was 12 kW, the Ar flow rate was 20 sccm, and the N_2 flow rate was 70 sccm. The substrate was kept at 150°C during deposition, and the film thickness was verified using spreading sheet resistance.

Both samples were then patterned using electron beam lithography at 100 kV accelerating voltage. Hexamethyldisilazane (HMDS) was first used to pre-treat the surface of the samples before spin coating with hydrogen silsesquioxane (HSQ) resist.[54] HSQ is a spin-on glass, with excellent etch resistance and resolution, that has been used extensively in electron beam lithography over the past two decades. A 3 mm x 3 mm area was patterned with a square array of circles, which was written with a 250 nm pitch and a 70 nm diameter. The resist was exposed with a dose of 3200 μC/cm^2, and was developed for 120 seconds at room temperature in MF-26A (Rohm and Haas Electronic Materials), which is an ammonium

hydroxide-based developer. Finally, samples were plasma etched using a 1200 W plasma with a 145 W bias and a 12 mTorr chamber pressure. The flow rates for the chlorine, boron trichloride, nitrogen, and argon were 100, 40, 20 and 100 sccm, respectively. *In-situ* end-point detection was used to stop each etch once the top aluminum layer was removed.

Finally, we should note that the 20 nm thick titanium nitride layer was not added for any optical purpose. This layer served as a protective coating between the underlying aluminum and the ammonium hydroxide used to develop the HSQ resist. Samples fabricated without this layer were destroyed during the resist development step.

REFERENCES

1.   Zeman, E. J.; Schatz, G. C. An accurate electromagnetic theory study of surface enhancement factors for Ag, Au, Cu, Li, Na, Al, Ga, In, Zn, and Cd. *Journal of Physical Chemistry* 1987, 91, 634-43.
2.   Sobhani, A.; Manjavacas, A.; Cao, Y.; McClain, M. J.; García de Abajo, F. J.; Nordlander, P.; Halas, N. J. Pronounced Linewidth Narrowing of an Aluminum Nanoparticle Plasmon Resonance by Interaction with an Aluminum Metallic Film. *Nano Letters* 2015, 15, 6946-6951.
3.   Taguchi, A.; Saito, Y.; Watanabe, K.; Yijian, S.; Kawata, S. Tailoring plasmon resonances in the deep-ultraviolet by size-tunable fabrication of aluminum nanostructures. *Applied Physics Letters* 2012, 101.
4.   Diest, K.; Liberman, V.; Lennon, D. M.; Welander, P. B.; Rothschild, M. Aluminum plasmonics: Optimization of plasmonic properties using liquid-prism-coupled ellipsometry. *Optics Express* 2013, 21, 28638-28650.
5.   Maidecchi, G.; Gonella, G.; Proietti Zaccaria, R.; Moroni, R.; Anghinolfi, L.; Giglia, A.; Nannarone, S.; Mattera, L.; Dai, H.-L.; Canepa, M.; Bisio, F. Deep ultraviolet plasmon resonance in aluminum nanoparticle arrays. *ACS Nano* 2013, 7, 5834-5841.
6.   Martin, J.; Proust, J.; Gerard, D.; Plain, J. Localized surface plasmon resonances in the ultraviolet from large scale nanostructured aluminum films. *Optical Materials Express* 2013, 3, 954-959.
7.   Ayas, S.; Topal, A. E.; Cupallari, A.; Guner, H.; Bakan, G.; Dana, A. Exploiting Native Al2O3for Multispectral Aluminum Plasmonics. *ACS Photonics* 2014, 1, 1313-1321.

8.   Bisio, F.; Proietti Zaccaria, R.; Moroni, R.; Maidecchi, G.; Alabastri, A.; Gonella, G.; Giglia, A.; Andolfi, L.; Nannarone, S.; Mattera, L.; Canepa, M. Pushing the high-energy limit of plasmonics. *ACS Nano* 2014, 8, 9239-9247.

9.   Knight, M. W.; King, N. S.; Liu, L.; Everitt, H. O.; Nordlander, P.; Halas, N. J. Aluminum for plasmonics. *ACS Nano* 2014, 8, 834-840.

10.   Norek, M.; Wlodarski, M.; Stepniowski, W. J. Tailoring of UV/violet plasmonic properties in Ag, and Cu coated Al concaves arrays. *Applied Surface Science* 2014, 314, 807-814.

11.   Liu, H.-W.; Lin, F.-C.; Lin, S.-W.; Wu, J.-Y.; Chou, B.-T.; Lai, K.-J.; Lin, S.-D.; Huang, J.-S. Single-Crystalline Aluminum Nanostructures on a Semiconducting GaAs Substrate for Ultraviolet to Near-Infrared Plasmonics. *ACS Nano* 2015, 9, 3875-3886.

12.   Martin, J.; Plain, J. Fabrication of aluminium nanostructures for plasmonics. *Journal of Physics D: Applied Physics* 2015, 48.

13.   McPeak, K. M.; Jayanti, S. V.; Kress, S. J. P.; Meyer, S.; Iotti, S.; Rossinelli, A.; Norris, D. J. Plasmonic films can easily be better: Rules and recipes. *ACS Photonics* 2015, 2, 326-333.

14.   Lecarme, O.; Sun, Q.; Ueno, K.; Misawa, H. Robust and Versatile Light Absorption at Near-Infrared Wavelengths by Plasmonic Aluminum Nanorods. *ACS Photonics* 2014, 1, 538-546.

15.   Ramadurgam, S.; Lin, T.-G.; Yang, C. Aluminum plasmonics for enhanced visible light absorption and high efficiency water splitting in core-multishell nanowire photoelectrodes with ultrathin hematite shells. *Nano Letters* 2014, 14, 4517-4522.

16.   Ramadurgam, S.; Chen, Y. In *Aluminum and copper plasmonics for enhancing internal quantum efficiency of core-shell and core-multishell nanowire photoelectrodes*, Nanophotonic Materials XI, 20-21 Aug. 2014, USA, SPIE - The International Society for Optical Engineering: USA, 2014; p 91610J (7 pp.).

17.   Abdulrahman, R. B.; Cansizoglu, H.; Cansizoglu, M. F.; Herzog, J. B.; Karabacak, T. Enhanced light trapping and plasmonic properties of aluminum nanorods fabricated by glancing angle deposition. *Journal of Vacuum Science and Technology A: Vacuum, Surfaces and Films* 2015, 33.

18.   Kai, L.; Suhua, J.; Dengxin, J.; Xie, Z.; Nan, Z.; Haomin, S.; Yun, X.; Qiaoqiang, G. Super Absorbing Ultraviolet Metasurface. *Photonics Technology Letters, IEEE* 2015, 27, 1539-1542.

19.   Lee, M.; Kim, J. U.; Lee, K. J.; Ahn, S.; Shin, Y.-B.; Shin, J.; Park, C. B. Aluminum Nanoarrays for Plasmon-Enhanced Light Harvesting. *ACS Nano* 2015, 9, 6206-6213.

20.   Tittl, A.; Michel, A.-K. U.; Schaferling, M.; Yin, X.; Gholipour, B.; Cui, L.; Wuttig, M.; Taubner, T.; Neubrech, F.; Giessen, H. A Switchable Mid-Infrared Plasmonic Perfect Absorber with Multispectral Thermal Imaging Capability. *Advanced Materials* 2015, 27, 4597-4603.

21.   Sigle, D. O.; Perkins, E.; Baumberg, J. J.; Mahajan, S. Reproducible deep-UV SERRS on aluminum nanovoids. *Journal of Physical Chemistry Letters* 2013, 4, 1449-1452.

22.   Norek, M.; Wlodarski, M.; Matysik, P. UV plasmonic-based sensing properties of aluminum nanoconcave arrays. *Current Applied Physics* 2014, 14, 1514-1520.

23.   Golmohammadi, S.; Ahmadivand, A. Fano Resonances in Compositional Clusters of Aluminum Nanodisks at the UV Spectrum: a Route to Design Efficient and Precise Biochemical Sensors. *Plasmonics* 2014, 9, 1447-56.

24.   Barrios, C. A.; Canalejas-Tejero, V.; Herranz, S.; Moreno-Bondi, M. C.; Avella-Oliver, M.; Puchades, R.; Maquieira, A. Aluminum Nanohole Arrays Fabricated on Polycarbonate for Compact Disc-Based Label-Free Optical Biosensing. *Plasmonics* 2014, 9, 645-9.

25.   Zheng, B. Y.; Wang, Y.; Nordlander, P.; Halas, N. J. Color-selective and CMOS-compatible photodetection based on aluminum plasmonics. *Advanced Materials* 2014, 26, 6318-6323.

26.   Ren, F.-F.; Ang, K.-W.; Ye, J.; Yu, M.; Lo, G.-Q.; Kwong, D.-L. Split bull's eye shaped aluminum antenna for plasmon-enhanced nanometer scale germanium photodetector. *Nano Letters* 2011, 11, 1289-1293.

27.   Tan, S. J.; Zhang, L.; Zhu, D.; Goh, X. M.; Wang, Y. M.; Kumar, K.; Qiu, C.-W.; Yang, J. K. W. Plasmonic color palettes for photorealistic printing with aluminum nanostructures. *Nano Letters* 2014, 14, 4023-4029.

28. Shrestha, V. R.; Lee, S.-S.; Kim, E.-S.; Choi, D.-Y. Aluminum plasmonics based highly transmissive polarization-independent subtractive color filters exploiting a nanopatch array. *Nano Letters* 2014, 14, 6672-6678.

29. Huang, Y.-W.; Chen, W. T.; Tsai, W.-Y.; Wu, P. C.; Wang, C.-M.; Sun, G.; Tsai, D. P. Aluminum plasmonic multicolor meta-Hologram. *Nano Letters* 2015, 15, 3122-3127.

30. Malhat, H. A.; Eltresy, N. A.; Zainud-Deen, S. H.; Awadalla, K. H. Reflectarray nano-dielectric resonator antenna using Different metals. *Applied Computational Electromagnetics Society Journal* 2015, 30, 967-974.

31. Ma, Y.-Q.; Shao, J.-H.; Zhang, Y.-F.; Lu, B.-R.; Zhang, S.-C.; Sun, Y.; Qu, X.-P.; Chen, Y.-F. Design and fabrication of structural color by local surface plasmonic meta-molecules. *Chinese Physics B* 2015, 24.

32. Eizner, E.; Avayu, O.; Ditcovski, R.; Ellenbogen, T. Aluminum Nanoantenna Complexes for Strong Coupling between Excitons and Localized Surface Plasmons. *Nano Letters* 2015, 15, 6215-6221.

33. Cheng, L.; Huang, L.; Li, X.; Wu, J.; Zhang, Y.; Wang, J.; Cheng, L.; Liu, Y.; Feng, X.; Zhang, W.; Cai, Y. UV plasmonic resonance of aluminum shallow pit arrays. *Journal of Physical Chemistry C* 2015, 119, 14304-14311.

34. Zhu, J.; Li, J.-J.; Zhao, J.-W. Tuning the plasmon band number of aluminum nanorod within the ultraviolet-visible region by gold coating. *Physics of Plasmas* 2014, 21.

35. Ross, M. B.; Schatz, G. C. Aluminum and indium plasmonic nanoantennas in the ultraviolet. *Journal of Physical Chemistry C* 2014, 118, 12506-12514.

36. Schwab, P. M.; Moosmann, C.; Wissert, M. D.; Schmidt, E. W. G.; Ilin, K. S.; Siegel, M.; Lemmer, U.; Eisler, H.-J. Linear and nonlinear optical characterization of aluminum nanoantennas. *Nano Letters* 2013, 13, 1535-1540.

37. Saito, Y.; Honda, M.; Watanabe, K.; Taguchi, A.; Yujian, S.; Kawata, S. Design of Aluminum Nanostructures for DUV Plasmonics: Blue Shifts in Plasmon Resonance Wavelength by Height Control. *Journal of the Japan Institute of Metals and Materials* 2013, 77, 27-31.

38. Knight, M. W.; Liu, L.; Wang, Y.; Brown, L.; Mukherjee, S.; King, N. S.; Everitt, H. O.; Nordlander, P.; Halas, N. J. Aluminum plasmonic nanoantennas. *Nano Letters* 2012, 12, 6000-6004.

39. Zoric, I.; Zach, M.; Kasemo, B.; Langhammer, C. Gold, platinum, and aluminum nanodisk plasmons: Material independence, subradiance, and damping mechanisms. *ACS Nano* 2011, 5, 2535-2546.

40. Langhammer, C.; Schwind, M.; Kasemo, B.; Zoric, I. Localized surface plasmon resonances in aluminum nanodisks. *Nano Letters* 2008, 8, 1461-1471.

41. Chu, Y.; Crozier, K. B. Experimental study of the interaction between localized and propagating surface plasmons. *Optics Letters* 2009, 34, 244-246.

42. Oates, T. W. H.; Dastmalchi, B.; Isic, G.; Tollabimazraehno, S.; Helgert, C.; Pertsch, T.; Kley, E.-B.; Verschuuren, M. A.; Bergmair, I.; Hingerl, K.; Hinrichs, K. Oblique incidence ellipsometric characterization and the substrate dependence of visible frequency fishnet metamaterials. *Optics Express* 2012, 20, 11166-11177.

43. Brakstad, T.; Kildemo, M.; Ghadyani, Z.; Simonsen, I. Dispersion of polarization coupling, localized and collective plasmon modes in a metallic photonic crystal mapped by Mueller Matrix Ellipsometry. *Optics Express* 2015, 23, 22800-22815.

44. Oates, T. W. H.; Wormeester, H.; Arwin, H. Characterization of plasmonic effects in thin films and metamaterials using spectroscopic ellipsometry. *Progress in Surface Science* 2011, 86, 328-376.

45. Tittl, A.; Harats, M. G.; Walter, R.; Yin, X.; Schäferling, M.; Liu, N.; Rapaport, R.; Giessen, H. Quantitative Angle-Resolved Small-Spot Reflectance Measurements on Plasmonic Perfect Absorbers: Impedance Matching and Disorder Effects. *ACS Nano* 2014, 8, 10885-10892.

46. Lodewijks, K.; Van Roy, W.; Borghs, G.; Lagae, L.; Van Dorpe, P. Boosting the Figure-Of-Merit of LSPR-Based Refractive Index Sensing by Phase-Sensitive Measurements. *Nano Letters* 2012, 12, 1655-1659.

47.   Quintanilha, R.; Thony, P.; Henry, D.; Hazart, J. In *3D features analysis using spectroscopic scatterometry*, Metrology, Inspection, and Process Control for Microlithography XVIII, 23-26 Feb. 2004, USA, SPIE-Int. Soc. Opt. Eng.: USA, 2004; pp 456-67.

48.   Lodewijks, K.; Ryken, J.; Van Roy, W.; Borghs, G.; Lagae, L.; Van Dorpe, P. Tuning the Fano Resonance Between Localized and Propagating Surface Plasmon Resonances for Refractive Index Sensing Applications. *Plasmonics* 2013, 8, 1379-1385.

49.   Liu, N.; Mesch, M.; Weiss, T.; Hentschel, M.; Giessen, H. Infrared Perfect Absorber and Its Application As Plasmonic Sensor. *Nano Letters* 2010, 10, 2342-2348.

50.   Jellison, G. E.; Modine, F. A. Two-modulator generalized ellipsometry: theory. *Appl. Opt.* 1997, 36, 8190-8198.

51.   Walsh, G. F.; Forestiere, C.; Dal Negro, L. Plasmon-enhanced depolarization of reflected light from arrays of nanoparticle dimers. *Optics Express* 2011, 19, 21081-21090.

52.   Bischoff, J. In *Improved diffraction computation with a hybrid C-RCWA-method*, 2009; pp 72723Y-72723Y-12.

53.   Pond, J.; Kleckner, T.; Paddon, P.; Reid, A. In *Emerging trends in photonics modeling*, Integrated Optics: Devices, Materials, and Technologies X, 23 Jan. 2006, USA, SPIE - The International Society for Optical Engineering: USA, 2006; pp 612306-1.

54.   Grigorescu, A. E.; Hagen, C. W. Resists for sub-20-nm electron beam lithography with a focus on HSQ: state of the art. *Nanotechnology* 2009, 20, 292001.